Near-Real-Time Detection of Tephra Eruption Onset and Mass Flow Rate Using Microwave Weather Radar and Infrasonic Arrays

Frank S. Marzano, *Fellow, IEEE*, Errico Picciotti, Saverio Di Fabio, Mario Montopoli, Luigi Mereu, Wim Degruyter, Costanza Bonadonna, and Maurizio Ripepe

***Abstract*—During an eruptive event, the near-real-time monitoring of volcanic explosion onset and its mass flow rate (MFR) is a key factor to predict ash plume dispersion and to mitigate risk to air traffic. Microwave (MW) weather radars have proved to be a fundamental instrument to derive eruptive source parameters. We extend this capability to include an early-warning detection scheme within the overall volcanic ash radar retrieval methodology. This scheme, called the volcanic ash detection (VAD) algorithm, is based on a hybrid technique using both fuzzy logic and conditional probability. Examples of VAD applications are shown for some case studies, including the Icelandic Grímsvötn eruption in 2011, the Eyjafjallajökull eruption in 2010, and the Italian Mt. Etna volcano eruption in 2013. Estimates of the eruption onset from the radar-based VAD module are compared with infrasonic array data. One-dimensional numerical simulations and analytical model estimates of MFR are also discussed and intercompared with sensor-based retrievals. Results confirm in all cases the potential of MW weather radar for ash plume monitoring in near real time and its complementarity with infrasonic array for early-warning system design.**

***Index Terms*—Detection algorithm, microwave (MW) remote sensing, volcanic ash, weather radar.**

Manuscript received December 8, 2015; revised March 27, 2016; accepted June 3, 2016. This work was supported in part by the FUTUREVOLC Project (Grant agreement no. 308377) within the European Union's FP7/2007-2013 program. The research leading to these results has also received funding from the APhoRISM project (Grant agreement no. 606738) within FP7/2007-2013 program.

F. S. Marzano and L. Mereu are with the Dipartimento di Ingegneria dell'Informazione (DIET), Sapienza Università di Roma, 00184 Rome, Italy, and also with the CETEMPS Center of Excellence, Università dell'Aquila, 67100 L'Aquila, Italy (e-mail: marzano@diet.uniroma1.it; mereu@diet.uniroma1.it).

E. Picciotti and S. Di Fabio are with the CETEMPS Center of Excellence, Università dell'Aquila, 67100 L'Aquila, Italy, and also with HIMET Srl, 67100 L'Aquila, Italy (e-mail: errico.picciotti@himet.it; saverio.difabio@aquila.infn.it).

M. Montopoli is with the Dipartimento di Ingegneria dell'Informazione (DIET), Sapienza Università di Roma, 00184 Rome, Italy, with the CETEMPS Center of Excellence, Università dell'Aquila, 67100 L'Aquila, Italy, and also with the Institute of Atmospheric Sciences and Climate (ISAC), National Research Council (CNR), 40129 Rome, Italy (e-mail: m.montopoli@isac.cnr.it).

W. Degruyter is with the Institute of Geochemistry and Petrology, Department of Earth Sciences, ETH Zurich, 8092 Zurich, Switzerland (e-mail: wim.degruyter@erdw.ethz.ch).

C. Bonadonna is with the Department of Earth Sciences, University of Geneva, 1205 Geneva, Switzerland (e-mail: Costanza.Bonadonna@unige.ch).

M. Ripepe is with the Dipartimento di Scienze della Terra, University of Florence, 50121 Florence, Italy (e-mail: maurizio.ripepe@unifi.it).

Color versions of one or more of the figures in this paper are available online at http://ieeexplore.ieee.org.

Digital Object Identifier 10.1109/TGRS.2016.2578282

I. Introduction

DURING an explosive volcanic eruption, tephra particles are injected into the atmosphere and may severely affect air traffic and local environment, as clearly demonstrated by the Icelandic 2010 Eyjafjallajökull eruption [1]–[3]. For prevention and protection needs, a key issue is to deliver a prompt early warning of the on-going volcanic eruption and to estimate the mass flow rate (MFR) to properly initialize ash dispersion forecasting models [4]–[6]. Satellite radiometry is a well-established method for the dispersed ash plume detection and monitoring [7]. However, estimates from spaceborne visible–infrared radiometers may be limited, depending on the sensor and platform, to daylight periods, few overpasses per day, optically thin ash clouds, and, if present, obscured by water clouds [8], [9].

Complementary to satellite sensors, a ground-based microwave (MW) weather radar represents nowadays a well-established technique to monitor quantitatively a volcanic eruption and its tephra ejection [10]–[12]. Weather radars can provide a 3-D volume of eruption source parameters (e.g., plume height, particle size distribution, and MFR) as well as mass concentration and velocity fields at any time during the day or night with a periodicity of 5–15 min and a spatial resolution less than a kilometer even in the presence of water clouds [13], [14]. The major limitations of plume radar retrieval are its limited spatial coverage (e.g., less than 150 km radius around the radar site), its poor sensitivity to fine ash particles (e.g., less than a diameter of 50 μm), and the relatively long time for completing a volume scan (order of several minutes). This implies, for example, that the top of the ash column above the emission source might be only partially detected, and the extension of the horizontally spreading plume may be underestimated and tracked for a relatively short distance [15], [39].

For a quantitative estimation of ash, an algorithm, called volcanic ash radar retrieval (VARR), has been developed in the recent years using radar systems operating at S-, C-, and X-bands at single and dual polarization [16], [17]. Note that, even though the acronym VARR refers to ash estimation by MW radars, the latter are, in general, sensitive to all tephra fragments, including lapilli (2–64 mm) and blocks and bombs (>64 mm). However, the term "ash" is so widely exploited that we will use it in place of tephra, thus intending all volcanic particles injected into the atmosphere irrespective of

0196-2892 © 2016 IEEE. Personal use is permitted, but republication/redistribution requires IEEE permission.
See http://www.ieee.org/publications_standards/publications/rights/index.html for more information.

size, shape, and composition, if not otherwise specified. The VARR theoretical background, application, and validation have been extensively described in previous works [12]. One key issue, which is still open, is its extension to the detection of ash plume onset in order to be used within an early-warning system for volcanic hazard prediction. In this respect, weather radars can be complementary to the other early-warning instruments like tremor detection networks, cloud detections based on Global Positioning System receiver networks, thermal and visible cameras, and infrasonic arrays (e.g., [18], [19], and [25]). In particular, an infrasonic airwave, produced by volcanic eruptions (usually at frequencies lower than 20 Hz), can be detected as an atmospheric pressure field variation also at remote distances [20]–[22]. Arrays of infrasonic sensors, deployed as small aperture ($\sim$100 m) antennas and distributed at various azimuths around a volcano, show a tremendous potential for enhanced event detection and localization. At short distances (<10 km) from the source, the almost constant velocity of sound makes precise localization (within a few tens of meters of accuracy) possible. With respect to other systems, infrasound (IS) is also largely unaffected by cloud cover and does not rely on line-of-sight view of vents (e.g., [19] and [25]), as is the case with satellite or radar observations.

The goal of this work is to extend VARR by including a volcanic ash detection (VAD) module and designing an overall scheme for ash plume monitoring in near real time providing eruption onset time, plume tracking, and geophysical products. The focus is on the methodological issues more than its statistical validation so that examples of VAD application are shown for specific test cases. Using data from recent volcanic eruptions, time series of infrasonic array and radar acquisitions in the proximity of the volcanic vent are used together to understand the potentiality of combining the two ground-based measurements for eruption onset early warning. Detection and estimation of MFR are also evaluated and compared with estimates from analytical equations, 1-D volcanic plume models, and IS-based methods.

The basic idea of VAD is that, during standard operations, the radar algorithm is set into a "meteorological mode" (devoted to monitoring precipitating water cloud echoes), but a special processing is envisaged at the locations where potentially active volcanoes are present within the radar coverage area. VAD continually runs for each radar volume acquisition. Whenever the VAD detection test is passed (i.e., an eruption is confirmed from VAD radar data analysis), the VARR data processing switches into an "ash mode," and the tracking module is activated (manually or automatically depending on the system). Note that near-real-time tracking of volcanic cloud dispersal represents an essential datum both for aviation and civil safety. Early-warning advisory can be spread to the local authorities if the ash plume trajectory threatens some sensitive areas (e.g., airports, aviation routes, critical infrastructures, towns, and metropolitan regions). In addition, the indication of the velocity of the transported plume provided by the tracking module can be a useful and alternative way for the retrieval of the plume altitude given the knowledge of the velocity–altitude profile obtained, for example, by radiosoundings and/or meteorological forecasts.

This paper is organized as follows. Section II will provide an overview of VARR block diagram, including the VAD module. The latter will be described in detail using a hybrid fuzzy logic and conditional probability approach. By exploiting available data, Sections III and IV will show examples of VAD applications for the Icelandic Grímsvötn eruption that occurred in 2011 and the Italian Mt. Etna volcano eruption that occurred in 2013. In the latter event, radar-based retrievals will be compared with infrasonic array data to interpret the respective signatures and explore their synergy. In Section V, VARR-based retrievals of the MFR at the vent will be analyzed for the May 5–10 period of the 2010 Eyjafjallajökull eruption by comparing them with estimates from the 1-D numerical model, analytical formula, and infrasonic array. Section VI will draw the conclusion and future work recommendations.

II. Designing VARR

The objective of this section is to illustrate an overall algorithm for MW weather radar polarimetric retrieval of volcanic ash plumes, including four major stages: detection, tracking, classification, and estimation of ash (i.e., in our context, all volcanic particles injected into the atmosphere irrespective of size, shape, and composition). The underlying concepts will be illustrated by sketching the underpinning philosophy and the basic theory, referring to previous works where possible for the discussion of tracking, classification, and estimation modules [12]. Only the detection module will be described in detail in Section II-B since it is the innovative module of this work.

The basic assumption in this work is that, in a given radar site, we have at disposal a set of variables at a specific frequency band (e.g., S-, C-, and X-bands) at single or dual polarization with a given range, azimuth, and elevation resolution (e.g., 250 m, 1°, and 1°, respectively). The latter defines the so-called radar resolution bin, and for each bin, we can introduce a polarimetric radar observable vector $\mathbf{z}_m = [Z_{hhm}, Z_{drm}, K_{dpm}, \rho_{hv}, L_{drm}]$, where Z_{hhm} is the measured copolar reflectivity factor, Z_{drm} is the differential reflectivity, K_{dpm} is the differential phase shift, ρ_{hv} is the copolar correlation (modulus) coefficient, and L_{drm} is the linear depolarization ratio. Since the availability of all of these observables is not always guaranteed, depending on the system capability, some of them can be discarded from the analysis, thus impacting the estimation accuracy. Details on the exploitation of dual-polarization and single-polarization radar systems can be found in [17] and [23]. All modules of VARR are supposed to operate on a volume-bin basis, whereas the use of spatial texture processing is foreseen but not discussed here.

A. Overall VARR Scheme

The VARR algorithm for polarimetric MW radars is, in a very general context, structured in the following four main modules, shown in Fig. 1.

1) VAD is detecting the ash plume onset from measured $\mathbf{z}_m$. The VAD algorithm is mainly devoted to characterizing the typical ash radar signature, possibly separating the

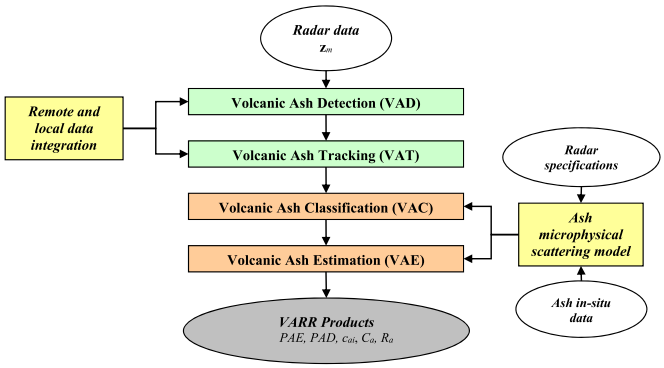

Fig. 1. At each time step and for each radar bin, VARR can provide probability of ash eruption PAE (in percent) and detection PAD (in percent), ash classification c_{ai} [i.e., mean particle diameter D_n (in millimeters)], ash mass concentration C_a (in grams per cubic meter), and ash fall rate R_a (in kilograms per square meter second). If Doppler capability is present, ash mean velocity v_{ma} (in meters per second) and ash velocity standard deviation σ_{va} (in meters per second) can be also estimated. Moreover, some other useful products could be derived, such as ash plume top height H_M (in meters), ash erupted volume V_a (in cubic meter), ash mass loading L_a (in kilograms per square meter), and ash MFR F_{Ra} (in kilograms per second).

radar bins affected by ash from those mainly interested by meteorological targets.

2) *Volcanic ash tracking* (VAT) is tracking the ash plume dispersion from measured $\mathbf{z}_m$ within the radar coverage area. The VAT algorithms are the basis of monitoring and nowcasting the displacement of the ash mass in space and time.
3) *Volcanic ash classification* (VAC) is classifying ash particle class from measured $\mathbf{z}_m$ within each radar bin in terms of particle's size, shape, and orientation. The VAC module is based on the maximum *a posteriori* probability (MAP) criterion trained by a forward particle MW scattering model.
4) *Volcanic ash estimation* (VAE) is estimating the ash concentration, fall rate, ash mean diameter, and other volcanic products from the measured $\mathbf{z}_m$ within each radar resolution bin.

Fig. 1 shows a flowchart of the VARR scheme. The VAD and VAT modules can be supported by the integration of other available measurements, e.g., remote sensing data from spaceborne infrared radiometers, ground-based infrasonic arrays, and lidars or *in situ* data, such as ash disdrometers or human inspections. On the other hand, the VAC and VAE modules are fed by the forward microphysical-electromagnetic scattering models ingesting information about weather radar instrumental characteristics and possible *in situ* sampling of previous eruptions.

The VAD module will be described in the next section, being the main objective of this work.

The VAT module takes as input the detection of the ash plume target and tracks it in time and space. In order to accomplish this task, a phase-based correlation technique (PCORR), well described in [24] and here only summarized, is used for this purpose. In order to estimate the displacement field, the PCORR algorithm exploits the comparison between two consecutive radar images, typically the constant altitude plan position indicator (PPI) but applicable to any radar observed or estimated field F_{rad}. The displacement field is expressed by the horizontal motion vector $\mathbf{V}(x, y)$ for each position (x, y) in the horizontal plane and whose Cartesian components $u(x, y)$ and $v(x, y)$ are used within an advection scheme to forecast the next radar image [24], [41]

$$\hat{F}_{\mathrm{rad}}(x, y, t + n\Delta t) = F_{\mathrm{rad}}(x - u \cdot n\Delta t, y - v \cdot n\Delta t, t) \quad (1)$$

where t is the current time, Δt is the time step of radar acquisition (e.g., 5, 10, or 15 min), and $n\Delta t$ is the lead time with respect to current time (e.g., 30 or 60 min in advance). The estimate of u and v components is carried out by computing the normalized Fourier transform of the spatial cross-correlation function $S_{Fcx}(\Delta x, \Delta y)$ and by extracting the spatial shift $(\Delta x, \Delta y)$ from the phase component of S_{Fcx}.

The frequency-domain approach improves the accuracy of motion directions and magnitude estimates by avoiding saturation effects in proximity of the correlation function multiple maxima. The limitations of PCORR, applied as described, are the following: 1) when applied to the whole radar image, it can provide only one motion vector per image, thus implicitly supposing a steady-state field, and 2) sources and sinks of radar observables are not considered so that the field is displaced but not modified in its value. These issues can be partially addressed by resorting to a spatially adaptive segmentation of the observed radar field to generate a spatially variable advection field. This approach can forecast the rotation and deformation of the observed field and has been successfully applied to atmospheric precipitation on a relatively large scale, even though physical models of sources and sinks are not taken into account [41]. By comparing the nowcasted and actual reflectivity maps, the accuracy of the predicted field decreases, as expected, with the increase of the lead time $n\Delta t$; percentage errors of 75% can be typically obtained at 0.5 h and of 60% at 1 h, but a detailed analysis is beyond the scopes of this work.

The VAC module is widely described in [16] and [17] and here only summarized. Ash category classification is carried out by applying the Bayesian theory in a supervised manner, i.e., we evaluate the posterior probability density function (pdf) by using the forward microphysical scattering model [16], [12]. When maximizing the posterior pdf, the method is called MAP, and the estimated ash class c_a at each time step and radar bin is expressed by [16]

$$\begin{aligned}\hat{c}_a &= \mathrm{Mode}_c\left\{p(c_a|\boldsymbol{z}_m)\right\} \\ &= \mathrm{Mode}_c\left\{p(\boldsymbol{z}_m|c_a)p(c_a)/p(\boldsymbol{z}_m)\right\}\end{aligned} \quad (2)$$

where p represents the pdfs, Mode_c is the modal operator, and $\mathbf{z}_m$ is the polarimetric radar observable vector, with $p(c_a|\boldsymbol{z}_m)$, $p(\boldsymbol{z}_m|c_a)$, and $p(c_a)$ being the posterior, likelihood, and *a priori* pdfs, respectively. The ash class c_a is usually provided in terms of size (i.e., fine ash: < 63 μm, coarse ash: 63 μm–2 mm, and lapilli: 2–64 mm together with blocks and bombs larger than 64 mm) and mass concentration category (e.g., low: average around 0.1 g/m^3, medium: average around 1 g/m^3, and high: average around 5 g/m^3). The *a priori* pdf $p(c_a)$ is used to insert available information on the requirements that make the existence of the class c_a likely in a given environmental condition. The *a priori* pdf is typically set uniform unless there

is evidence of prevailing ash class. A usual simplifying assumption of MAP is to introduce a multidimensional Gaussian pdf model in order to reduce (2) to the minimization of quadratic metrics, i.e., the squared generalized distance between the available polarimetric measurement and the corresponding class centroids, obtained from the forward microphysical scattering model [16]. The advantage of a supervised Bayesian approach is the flexibility and rigorousness to deal with all data, but on the other hand, it strongly relies on the accuracy of the forward training model.

The VAE module is well described in [12], [16], and [17] so that here it is only summarized. The Bayesian approach can be also used, in principle, for the estimation of physical source parameters. In case we are able to assume a function model f_{est} to relate the predicted parameter with available measurements, then the Bayesian method reduces to statistical regression so that the estimated volcanic ash parameter P_a is expressed by [17]

$$\hat{P}_a = f_{\text{est}}(\boldsymbol{z}_m; \boldsymbol{r}|\hat{c}_a) \tag{3}$$

where $\boldsymbol{r}$ is the vector of unknown regression coefficients which are found by a minimum least square technique, conditioned to estimated ash category c_a. The latter is again found by resorting to the forward training model with all potential and limitations discussed for VAC. The choice of the functional relationship may be critical, but on the other hand, it greatly simplifies the estimation step and makes it computationally very efficient. A power-law regression model can be chosen for ash mass concentration and fall rate for (3) [16], [17]. As listed in Fig. 1, at each time step and for each radar bin, VAE can provide ash mass concentration C_a (in grams per cubic meter), ash fall rate R_a (in kilograms per square meter second), and mean particle diameter D_n (in millimeters). If Doppler capability is present and proper algorithms are applied such velocity-azimuth display [42], ash mean velocity v_{ma} (in meters per second) and ash velocity standard deviation σ_{va} (in meters per second) in both horizontal and vertical directions can also be estimated [44]. Moreover, some other products can be derived from the overall volume analysis at each time step, such as ash plume top height H_M (in meters), ash plume volume V_a (in cubic meters), ash mass loading L_a (in kilograms per square meter), and ash MFR F_{Ra} (in kilograms per second). The latter is described in Section V-A.

B. VAD Module

Detection of ash clouds is a cumbersome problem as their signature can be confused, from an MW radar point of view, with hydrometeor features. In this paragraph, a methodology is presented for the real-time automated identification of volcanic solid particle emissions, based on the availability of weather radar data every Δt minutes. The detection (or monitoring) method here discussed exploits the analysis of copolar reflectivity measurements associated to geographical digital information. This is justified by the fact that most operational radar systems are single polarization only so that this choice implies the applicability of our VAD methodology to all weather radars currently used for volcano monitoring. Its generalization to polarimetric radar data is beyond the scopes of this work, but it is, of course, feasible [17]. The proposed scheme for monitoring and tracking ash plumes is presented in Fig. 2.

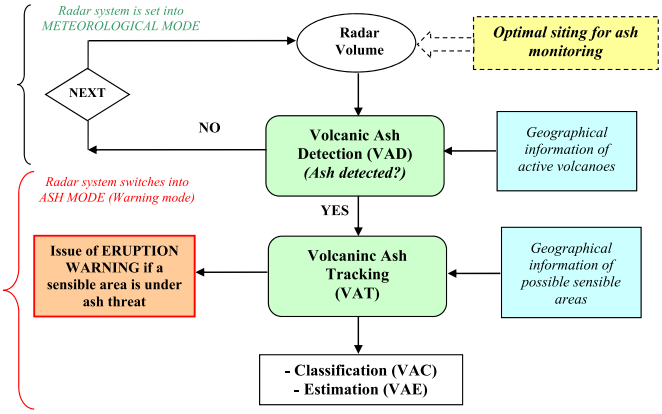

Fig. 2. Schematic block diagram for ash detection (VAD) coupled with tracking (VAT), classification (VAC), and estimation (VAE) modules. Radar 3-D volumes are available typically every 5, 10, or 15 min, depending on the range-elevation-azimuth scanning schedule and system specifications.

As described in Section II-A, weather radar data can be integrated with information received from different available sources, such as remote sensors from ground stations, space platform, and the Volcanic Aviation Advisory Center bulletin. The efficacy of radar detection and tracking of ash plumes is, of course, conditioned by the optimal choice of radar site, which may limit the volcanic vent MW visibility.

The VAD algorithm is designed for the following: 1) to keep pace with real-time data and to provide a detection result at the end of each radar volume acquisition (as fast as possible in order to follow the eruption dynamics) and 2) to store previous acquired data (at least 1 h), to be maintained in a database in order to allow further analyses if needed. Radar algorithms can usually be applied to measurements represented in native spherical coordinates or to data in resampled Cartesian coordinates, which allows a simpler geometrical interpretation. The VAD algorithm, instead of using the radar 3-D volume, is applied to a bidimensional (2-D) product, such as the vertical maximum intensity (VMI) which is the maximum value of measured reflectivity along the column at each Cartesian ground pixel (x, y) or $(i.j)$ in its discrete form. The advantage of considering VMI is the reduction of the processing complexity, making VAD computationally more efficient. In addition, since VMI privileges the reflectivity peaks that are present in a radar volume, it results more suitable for hazard warning. Obviously, all noise contaminations in radar volumes (e.g., ground clutter, second trip echoes, and anomalous propagation effects) must be filtered out in order to efficiently discriminate atmospheric targets. The VAD technique should use the appropriate scan strategy (i.e., the number of elevation-azimuth angles) that is a critical decision during operational use. The choice shall depend on the distance between the volcano and the radar and on the heights of radar beams with respect to the surface.

The VAD algorithm starts splitting the coverage area, where all potentially active volcano vents are located, in three (or more) concentric circular sectors arbitrarily centered on the volcano location. As an example, Fig. 3 shows how the sectors are subdivided for the Mt. Etna (left panel) and the Grímsvötn

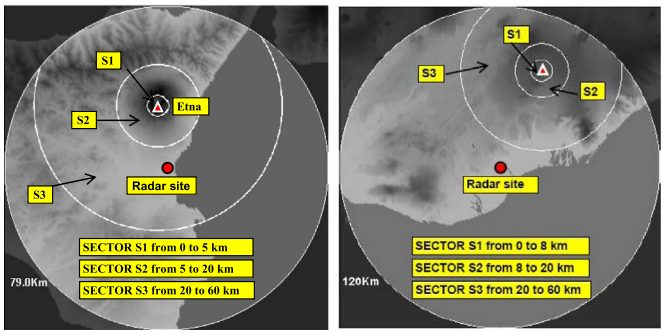

Fig. 3. Three sectors in which the Mt. Etna volcanic area (left panel) and Grímsvötn volcanic area (right panel) are subdivided. Circular sectors s_1, s_2, and s_3 have different radii in the two areas due to different setups, and within each of them, radar observables are processed by the VAD algorithm.

volcanic target area (right panel). Due to the diverse geographical characteristics and radar installations, the homologous sectors have different sizes in the two analyzed target areas. The basic idea is to mark each concentric circular sector s_k (e.g., $k = 1, 2, 3$) with the class labels $s_k =$ yes (Y) or $s_k =$ no (N), according to a hybrid fuzzy logic probabilistic strategy.

The block diagram of the VAD algorithm is structured along the following steps.

1) Define concentric circular sectors s_k of diameters $d_1 < \cdots < d_k < d_{k+1}$ within the radar maximum coverage area and centered on the volcano vent (typically $k = 3$).
2) Extract within these sectors s_k and at each discrete time step t_n the following features at each pixel $(i.j)$: a) the reflectivity VMI values $Z_M(s_k, i, j, t_n)$; b) the echo-top height values $H_M(s_k, i, j, t_n)$, which are the maximum height values where $Z_M(s_k, i, j, t_n) > S_{Zk}$ and where S_{Zk} is a proper threshold that is empirically derived; and c) the percentage $N_p(s_k, t_n)$ of N_k pixels of Z_M above the threshold signal S_{Zk} with respect to the total sector pixels $N_{\rm tot}(s_k)$ so that $N_p(s_k, t_n) = 100\ N_k/N_{\rm tot}(s_k)$, with N_k larger than a threshold signal S_{Zk}. This threshold is empirically set and may be site dependent (e.g., see Section III and Table I).
3) Convert each feature X (with $X = Z_M$, H_M, or N_p) into a membership probability using a ramp membership function $M_X[X; X_{\rm th}, \Delta X]$. The latter is defined as a function of the threshold parameter $X_{\rm th}$ and interval parameter ΔX so that

$$\begin{cases} M_X[X; X_{\rm th}, \Delta X] = 0 \text{ if } X < X_{\rm th} \\ M_X[X; X_{\rm th}, \Delta X] = 1 \text{ if } X > X_{\rm th} + \Delta X \\ M_X[X; X_{\rm th}, \Delta X] = \Delta X^{-1}(X - X_{\rm th}) \text{ elsewhere.} \end{cases} \quad (4)$$

The values of the thresholds and interval parameters depend on the radar scan strategy, distance volcano–radar, and their relative altitude, radar azimuth, and range resolution and circular sector topology (e.g., see Section III and Table I).
4) Define an inference rule function for each sector s_k as the product of the membership function of each feature X (*fuzzification stage*)

$$I_k[Z_M, H_M, N_p; s_k] = M_Z[Z_M] M_H[H_M] M_N[N_p]. \quad (5)$$

5) Assign a label "Y" (yes) or "N" (no) to each sector s_k at each time step t_n, taking the maximum of the inference rule function I_k and checking if it is greater or lesser than 0.5 (*defuzzification stage*)

$$\text{Max}_{i,j}\{I_k[Z_M, H_M, N_p; s_k]\} = \begin{cases} \geq 0,5 & \rightarrow S_k = Y \\ < 0,5 & \rightarrow S_k = N \end{cases} \quad (6)$$

where the maximum Max_{ij} is searched within all pixels (i, j) of sector k if the percentage number of pixels is above a given threshold S_{Nk} that is typically empirically derived.
6) Estimate a probability of ash eruption (PAE) at a given time step t_n by evaluating different temporal combinations for $s_k = Y$ or N at previous time steps t_{n-i} (with $i = 1 \div N_V$) as follows (*ash eruption conditional probability stage*):

$$\text{PAE}(t_n) = p_{\rm ash}(t_n, s_1 | s_2, s_3) p_{\rm avg}(\Delta t_n, s_1 | s_2, s_3) \quad (7a)$$

with

$$p_{\rm ash}(t_n, s_1 = Y | s_2, s_3) > 0$$
$$p_{\rm avg}(\Delta t_n, s_1 = Y | s_2, s_3) = \frac{1}{N_V} \sum_{i=1}^{N_V} p_{\rm ash}(t_{n-i}, s_1 | s_2, s_3)$$
$$p_{\rm ash}(t_n, s_1 = N | s_2, s_3) = 0 \quad (7b)$$

where $p_{\rm ash}(t_n, s_1 = Y | s_2, s_3)$ and $p_{\rm ash}(t_{n-i}, s_1 | s_2, s_3)$ are the ash conditional probabilities, respectively, at present instant t_n and at previous acquisition time steps t_{n-i} for a given class label combination in s_1, s_2, and s_3, whereas N_V is the number of volumes considered in previous acquisition time steps within the interval Δt_n. PAE in (7) is the product of two conditional probabilities of ash: the current probability of ash when in the inner sector $s_1 = Y$ and the temporal average of past probabilities in sector s_1, both conditioned to the outcomes of (5) in outer sectors s_2 and s_3. Note that the PAE value is computed automatically after every radar volume scan, and its value ranges from 0 to 1.

The time span Δt_n of the average probability $p_{\rm avg}$ is typically set to 1 h so that $N_V = \Delta t_n / \Delta t$, with Δt as the time step of radar acquisition. Both $p_{\rm ash}(t_n)$ and $p_{\rm ash}(t_{n-i})$ are empirically tunable probabilities, depending on the volcanic observation scenario and available information. These conditional probabilities are meant to discriminate ash plumes from meteorological storms, exploiting their different temporal evolutions. As an example, from the analysis of past case studies of volcanic eruptions in Iceland and Italy, Tables II and III provide, respectively, the conditional current and previous probability $p_{\rm ash}$ in (7), derived from label combinations in sectors 2 and 3 and depending on the label (Y or N) of sector 1. It is worth recalling that, if $s_1 = N$ at current instant t_n, the PAE value is set to zero automatically. The proposed values in the previous tables basically guarantee that volcanic ash is not detected in cases of persistent and/or widespread radar echoes, likely due to moving stratiform

TABLE I
PARAMETERS OF THE VAD MEMBERSHIP FUNCTIONS M_X, AS DESCRIBED IN (4), IN THE THREE SECTORS FOR THE 2011 GRÍMSVÖTN CASE STUDY

Symbol	Parameter	Units	Value in sector s_1 (k=1)	Value in sector s_2 (k=2)	Value in sector s_3 (k=3)
Z_{Mth}	VMI reflectivity	dBZ	20	20	15
ΔZ_M	VMI reflectivity interval	dBZ	10	10	10
H_{Mth}	Max altitude	km	0.8	1.4	1.4
ΔH_M	Max altitude interval	km	1	0.6	0.6
N_{pth}	Percentage pixel number threshold	%.	0	0	0
ΔN_p	Percentage pixel number interval	%.	100	40	10
S_{Zk}	VMI reflectivity threshold	dBZ	20	15	10
S_{Nk}	Pixel number threshold	Adim.	3	8	100
$N_{tot(Sk)}$	Total pixel number	Adim.	5021	26392	216384

TABLE II
CONDITIONAL PROBABILITY p_{ash} FOR SECTORS 2 AND 3 ONCE SECTOR 1 IS MARKED AS Y ($s_1 = Y$) AT PRESENT INSTANT t_n OR AT PREVIOUS INSTANTS t_{n-i}. NOTE THAT, IF $s_1 = N$ AT CURRENT INSTANT t_n, THE PAE VALUE IS SET TO ZERO AUTOMATICALLY. THE RATIONALE BEHIND IS THAT VOLCANIC ASH IS NOT DETECTED IN CASES OF PERSISTENT AND/OR WIDESPREAD RADAR ECHOES DUE TO METEOROLOGICAL CLOUDS

Label combination if s_1=Y	**Sector 3** labeled as s_3=**Y**	**Sector 3** labeled as s_3=**N**
Sector 2 labeled as s_2=**Y**	$p_{ash}(t_n, s_1=\mathrm{Y} \mid s_2=\mathrm{Y}, s_3=\mathrm{Y}) = 0.00$	$p_{ash}(t_n, s_1=\mathrm{Y} \mid s_2=\mathrm{Y}, s_3=\mathrm{N}) = 0.50$
Sector 2 labeled as s_2=**N**	$p_{ash}(t_n, s_1=\mathrm{Y} \mid s_2=\mathrm{N}, s_3=\mathrm{Y}) = 0.70$	$p_{ash}(t_n, s_1=\mathrm{Y} \mid s_2=\mathrm{N}, s_3=\mathrm{N}) = 1.00$

TABLE III
CONDITIONAL PROBABILITY p_{ash} FOR SECTORS 2 AND 3 ONCE SECTOR 1 IS MARKED AS N ($s_1 = N$) AT PREVIOUS INSTANTS t_{n-i}

Label combination if s_1=N	**Sector 3** labeled as s_3=**Y**	**Sector 3** labeled as s_3=**N**
Sector 2 labeled as s_2=**Y**	$p_{ash}(t_{n-i}, s_1=\mathrm{N} \mid s_2=\mathrm{Y}, s_3=\mathrm{Y}) = 0.00$	$p_{ash}(t_{n-i}, s_1=\mathrm{N} \mid s_2=\mathrm{Y}, s_3=\mathrm{N}) = 0.75$
Sector 2 labeled as s_2=**N**	$p_{ash}(t_{n-i}, s_1=\mathrm{N} \mid s_2=\mathrm{N}, s_3=\mathrm{Y}) = 0.65$	$p_{ash}(t_{n-i}, s_1=\mathrm{N} \mid s_2=\mathrm{N}, s_3=\mathrm{N}) = 1.00$

meteorological storms covering the outer sectors in the volcano surrounding. Convective rain clouds, developing close to the volcano vent as in many tropical volcanoes, might be confused with ash plumes. In this respect, radar polarimetry could help in refining the detection procedure. From our experience, for the Icelandic and Italian volcanic eruption cases, PAE ≥ 0.8 is associated to the presence of ash plumes, whereas PAE ≤ 0.6 is mainly due to meteorological targets. On this basis, as soon as sector 1 is labeled as Y, the PAE value is computed by means of (7).

7) Label the radar echoes around the potential volcanic vent in the inner sector s_1 at instant t_n by means of $L_{\mathrm{PAE}}(t_n, s_1)$, defined as (*ash eruption target labeling stage*)

$$L_{\mathrm{PAE}}(t_n, s_1) = \begin{cases} \text{Meteorological} & \text{if } 0 \leq \mathrm{PAE} < T_{E1} \\ \text{Uncertain} & \text{if } T_{E1} \leq \mathrm{PAE} < T_{E2} \\ \text{Ash} & \text{if } \mathrm{PAE} \geq T_{E2} \end{cases} \tag{8}$$

where T_{E1} and T_{E2} are proper thresholds, typically set to 0.6 and 0.8, respectively, as mentioned before.

8) The spatial identification of radar echoes, affected by ash, can be performed by introducing the probability of ash detection (PAD). The latter is an areal probability of detection applied to all pixels within the radar coverage estimated as (*ash detection conditional probability stage*)

$$\begin{aligned} \mathrm{PAD}(i, j, t_n) = \{ & w_z M_z \left[Z(i, j) \right] \\ & + W_H M_H \left[H_M(i, j) \right] \} M_D \left[d(i, j) \right] \end{aligned} \tag{9}$$

where the new membership function MD takes into account the distance between the pixel (i, j) and the volcano vent. Roughly speaking, (9) reveals the presence of ash in a given pixel if there is a suitable distance from the vent via d, if those pixels lie in a specified range of altitudes via H_M, and if the maximum reflectivity is sufficiently high via Z_M. PAD values are in the same range of the PAE; in (9), the weights w_z and w_H can be set to 0.5, but they can take into account the instantaneous availability of each source of information and its strength. The PAD formula in (9) may be enriched and improved by exploiting additional radar features, such as spatial texture and gradient of reflectivity, radial velocity, and some polarimetric features.

9) In similar fashion to (8), we can then define a radar detection label $L_{\mathrm{PAD}}(t_n, i, j)$, which has generally different thresholds T_{E3} and T_{E4}. The L_{PAD} label is introduced to discriminate among meteorological and ash in each pixel of the radar domain, taking into account any uncertain or mixed condition (*ash detection target labeling stage*)

$$L_{\mathrm{PAD}}(t_n, i, j) = \begin{cases} \text{Meteorological} & \text{if } 0 \leq \mathrm{PAD} < T_{E3} \\ \text{Uncertain} & \text{if } T_{E3} \leq \mathrm{PAD} < T_{E4} \\ \text{Ash} & \text{if } \mathrm{PAD} \geq T_{E4}. \end{cases} \tag{10}$$

If $L_{\mathrm{PAE}}(t_n, s_1) = \text{Ash}$, the VAD algorithm switches (automatically or semiautomatically) into a warning mode so that tracking (VAT), classification (VAC), and estimation (VAE) procedures can be activated. These modules are applied to (i, j) pixels, where $\mathrm{PAD}_k(i, j, t_n) \geq T_{E3}$, in order to keep pixels labeled as ash or as uncertain. The probability PAE

TABLE IV
CONDITIONAL PROBABILITY p_{ash} FOR SECTORS 2 AND 3 IF SECTOR 1 IS MARKED $s_1 = Y$ AT CURRENT AND PREVIOUS INSTANTS t_{n-i} AND IF PAE ≥ 0.80 (ASH ECHO)

Label combination if s_1=YES and PAE(t_{n-1}) seems to confirm an eruption	**Sector 3** labeled as s_3=**Y**	**Sector 3** labeled as s_3=**N**
Sector 2 labeled as s_2=**Y**	$p_{ash}(t_n,s_1=\mathrm{Y}\|s_2=\mathrm{Y},s_3=\mathrm{Y})=0.4$	$p_{ash}(t_n,s_1=\mathrm{Y}\|s_2=\mathrm{Y},s_3=\mathrm{N})=0.9$
Sector 2 labeled as s_2=**N**	$p_{ash}(t_n,s_1=\mathrm{Y}\|s_2=\mathrm{N},s_3=\mathrm{Y})=0.75$	$p_{ash}(t_n,s_1=\mathrm{Y}\|s_2=\mathrm{N},s_3=\mathrm{N})=1$

in (7), immediately after the ash detection instant t_n, must be evaluated with Table IV, instead of Table II, in order to verify if the volcanic ash eruption from the vent is a continuing phenomenon.

If $L_{\mathrm{PAE}}(t_n, s_1) =$ Uncertain, reflectivity echoes can be affected by false alarm or misdetection due to mixed phase (hydrometeor and ash signatures) or under particular atmospheric conditions.

If $L_{\mathrm{PAE}}(t_n, s_1) =$ Meteorological, VARR chain successive modules are not activated, and the detection cycle is updated to the next time step. Note that, if immediately after $L_{\mathrm{PAE}}(t_n, s_1) =$ Ash, then $s_1 = N$, PAE is set to zero, and probably a false alarm may have happened or it may behave intermittently. On the other hand, if the eruption stops after some time, dispersed ash will be detected only into outer sectors but not in the inner sector s_1. In these cases, VAT, VAC, and VAE are applied anyway to (i, j) pixels, where $\mathrm{PAD}(i, j, t_n) \geq T_{E3}$.

In summary, the probability of the volcanic eruption onset is described in time by the PAE time series evolution. Its behavior is an indicator of eruption column ejecting ash in the surrounding of the volcanic vent. On the other hand, the spatial discrimination between ash and meteorological radar echoes is performed by PAD maps. The efficiency of the latter is, of course, essential for any prompt and effective support to decision.

III. RADAR-BASED DETECTION OF VOLCANIC ERUPTION ONSET

The VAD algorithm has been tested for several volcanic eruptions and requires that a weather radar is available and operating during the eruption, which is not always the case when eruptions occur.

As an example, here we will show the results obtained from the volcanic eruption that occurred in May 2011 at the Grímsvötn volcano, located at the northwest of the Vatnajökull glacier in south-east Iceland (e.g., [27]). It is one of the most active Icelandic volcanoes. An explosive subglacial volcanic eruption started in the Grímsvötn caldera around 19:00 UTC on May 21, 2011. The strength of the eruption decreased rapidly, and the plume was below ∼10-km altitude after 24 h [40]. The eruption was officially declared over on May 28 at 07:00 UTC. More details on the Grímsvötn eruption observations and estimates can be found in [27] and [23] with a comprehensive analysis of the eruptive event from VAC and VAE results using polarimetric radar data at X-band.

The X-band dual polarization radar measurements (DPX) used in this study are acquired by the Meteor 50DX system which is a mobile compact weather radar deployed on

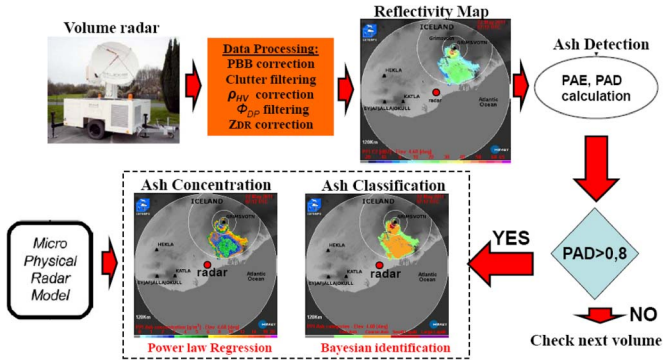

Fig. 4. VARR data processing flow diagram as applied to the 2011 Grímsvötn eruption case study (see text for details). Acronyms and symbols: PAE (probability of ash eruption), PAD (probability of ash detection), and PBB (partial beam blocking). Z_{hh} is the measured copolar reflectivity factor, Z_{dr} is the differential reflectivity, Φ_{dp} is the phase shift, and ρ_{hv} is copolar correlation (modulus).

a transportable trailer. For the volcanic event of May 2011 in Iceland, it has been positioned in the Kirkjubæjarklaustur, southern Iceland, at approximately 75 km from the Grímsvötn volcano [23]. During its operational activities in May 2011, DPX scans were set to 14 elevations angles from 0.7° to 40°. All polarimetric observables have range, azimuth, and time sampling of 0.20 km, 1°, and 10 min, respectively, and have been properly postprocessed to remove ground clutter and other impairments. A flow diagram of the VARR algorithm chain is shown in Fig. 4. The data processing steps, applied to this case study and here summarized, are well described in [23].

Three concentric circular sectors, centered at the Grímsvötn eruption vent, have been set up, having maximum ranges of 8, 20, and 60 km, respectively (see Fig. 3, right panel). The number of time steps N_V, to be used in (7), depends on the rate of radar scans; since in this case scans are every 10 min, then $N_V = 6$ within an hour. The results of VAD for this case study are shown in Figs. 5 and 6 on two time intervals on the third day as an example. PAE values have been computed using the processing chain of Section II since the beginning of eruption in different weather conditions. The label value (Y'' or "N") of each sector is also shown for completeness. The maximum values of the detected reflectivity, along the vertical column centered on (i, j), are projected on the surface as a PPI georeferenced radial map. The label VMI-CZ in these figures stands for VMI-corrected reflectivity, where the corrections are those usually related to ground clutter removal and Doppler dealiasing [42].

The ash plume is visible over the Grímsvötn volcano, especially looking at the sequence of Fig. 5 where strong reflectivity

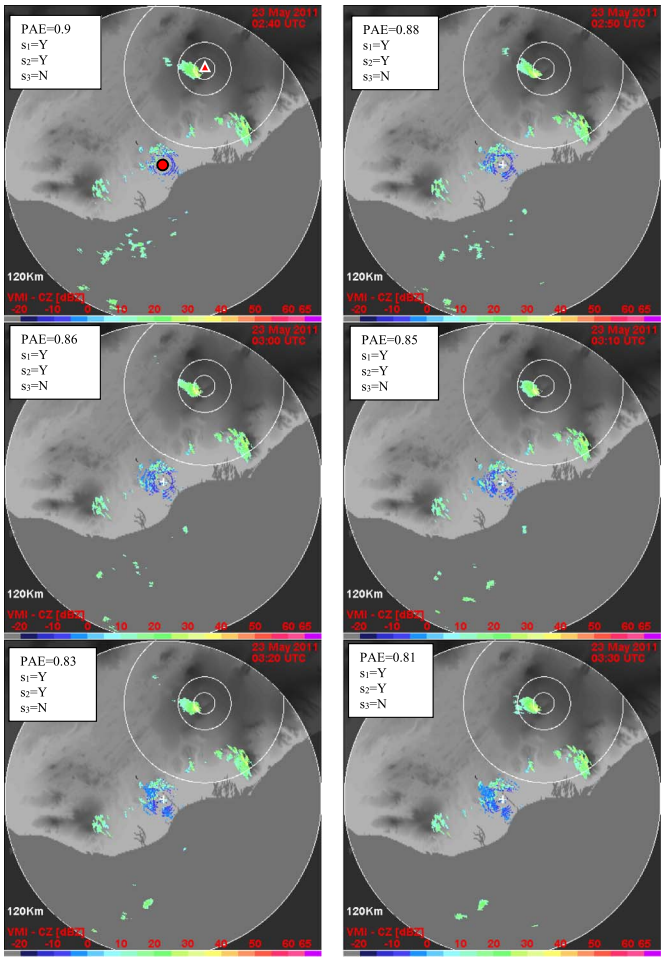

Fig. 5. VMI of corrected reflectivity (CZ), taken by Meteor 50DX on May 23 from 02:40 to 03:30 UTC during the 2011 Grímsvötn eruption. The radar and the volcano vent positions are indicated only in the first panel with the red circle and red triangle symbols, respectively. PAE and sector label values for each sector are also shown. Signals outside the s_1, s_2, and s_3 domains are mainly due to clutter.

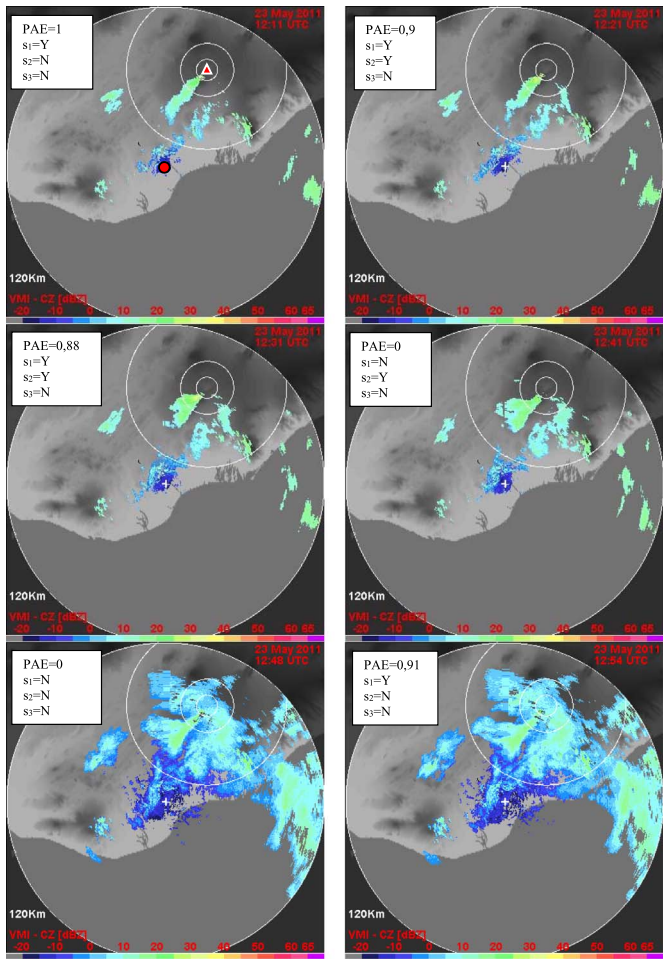

Fig. 6. Corrected VMI reflectivity images taken by Meteor 50DX on May 23 from 12:11 to 12:54 UTC during the 2011 Grímsvötn eruption. The radar and the volcano vent positions are indicated only in the first panel with the red circle and red triangle symbols, respectively. PAE and sector label values for each sector are also shown.

values are detected around the vent in clear-air conditions. On the contrary, Fig. 6 shows the sequence of PAE values in the presence of a small horizontally extended ash plume coexisting with other meteorological clouds in the outer sectors. The latter may cause false alarms, but the conditional check of all sectors avoids apparent detection errors. The detected volcanic plume is also distinguishable from undesired residual ground clutter returns, with the latter being recognizable as it tends to show a VMI stationary field from an image to another.

The temporal sequence of PAE, which might represent an operational warning product of VAD, is shown in Fig. 7 for whole days of May 24 and 25. In this figure, gray areas indicate the instants where we have found an ash plume by visual inspection of each radar scan. The colored circles in the PAD sequence refer to hit, false, and miss plume detection. The hit rate (green circles) is high, and this is an encouraging result for further tests. In the case of the 2011 Grímsvötn event, the observed temporal sequence definitely indicates a distinct ash feature erupted from the volcano vent, which can be effectively detected by means of the PAE product. Missed detection (i.e., observed but not detected by the PAE algorithm) is due to very

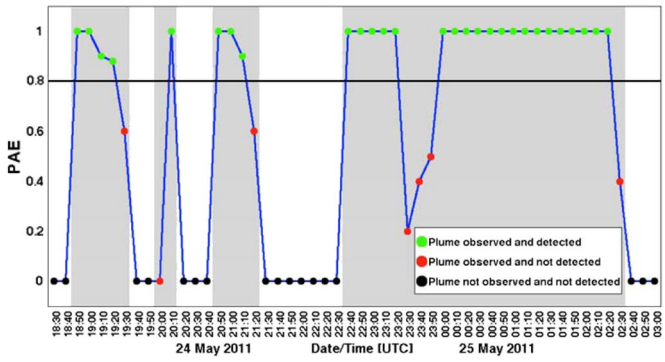

Fig. 7. Temporal sequence (sampled every 10 min) of PAE, extracted by VAD from X-band radar images on May 24–25, 2011, during the Grímsvötn eruption. Gray areas mark instants where *a posteriori* visual inspection confirmed the presence of the plume at the Grímsvötn volcano.

low reflectivity values around the volcano vent correlated to the small observed plume. False detection could instead occur when rain clouds, developing close to the volcano vent, are confused with ash plumes.

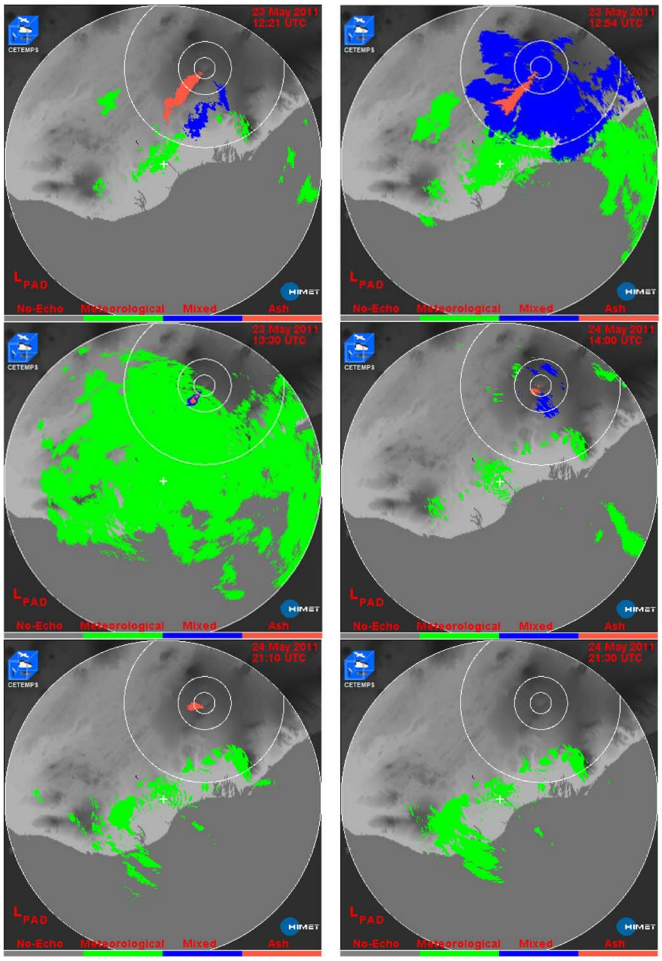

Fig. 8. Example of VAD results using the PAD label L_{PAD} for some eruption instants, selected considering different weather conditions during the 2011 Grímsvötn eruption.

Some examples of PAD results, computed by (9), are shown in Fig. 8 for some instants selected considering different weather conditions. The results are expressed using the radar detection label L_{PAD}, in (10), once setting the thresholds $T_{E3} = 0.6$ and $T_{E4} = 0.8$. As expected, in case of an ash eruption in clear air with strong reflectivity values, as in May 23 12:21 UTC, the PAD is set to *ash mode*. In the mixed scenario of May 23 13:30 UTC, the PAD changes into *uncertain mode*; it is worth noting that the residual ground clutter is classified as a meteorological target, as expected.

IV. Radar and IS Detection of Ash

MW weather radars can scan the whole atmosphere in a 3-D fashion in an area of about 10^5 km^2 [12]. The entire volume is accomplished in about 3–5 min depending on the number of elevation angles, azimuth angles, and range bins but also on the antenna rotation rate (which is typically of 3–6 rounds per min). This means that a single voxel (volume pixel) of the 3-D volume can only be sampled every few minutes. In this respect, an MW weather radar can benefit from the integration of other volcanic site measurements with a more rapid sampling but still sensitive to the onset of the ash eruption. This paragraph will explore this synergetic scenario.

The Mt. Etna volcano (Sicily, Italy) has produced more than 50 lava fountains since 2011 from a new crater formed

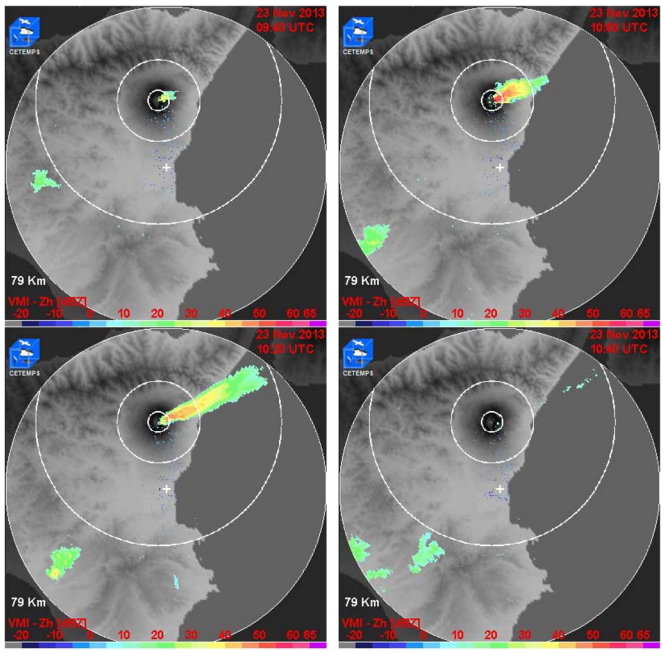

Fig. 9. VMI images, as derived from the X-band DPX radar system located at the Catania airport, during the Mt. Etna eruption on November 23, 2013. Only time steps at 9:40, 10:00, 10:20, and 10:40 UTC are shown for brevity.

in November 2009 [18], [25]. These events are characterized by the onset of Strombolian activity accompanied by volcanic tremor (resumption phase), an intensification of the explosions with the formation of an eruption column producing ash fallout (paroxysmal phase), and, finally, the decrease of both the explosion intensity and volcanic tremor (final phase) [20], [25].

The Mt. Etna eruption of November 23, 2013, was a lava fountain event more intense than usual which began in the afternoon of November 22, intensified after 07:00 UTC of November 23 [26]. The lava fountain was formed at 09:30 UTC and lasted up to 10:20 UTC, forming a magma jet up to about 1 km and an eruption plume higher than 9 km that dispersed volcanic ash toward the north-eastern volcano flanks [35]. The eruption ended at about 11:30 UTC.

This Mt. Etna eruption was observed by the same DPX X-band radar system, deployed in Iceland in 2011 (see Section III). In this case, the DPX radar is permanently positioned at the Catania airport (Sicily, Italy) at an altitude of 14 m and approximately 32 km far away from the Mt. Etna crater of interest (see Fig. 3(a), left panel). The DPX radar system works at 9.4 GHz and is operated to cover an area within a circle of 160 km radius every 10 min [23]. Fig. 9 shows the temporal samples of VMI imagery showing the onset of the lava fountain at 9:40 UTC, the intensification, and the dissipation around 10:40 UTC. Note that the ash plume is not detected by the DPX radar after 10:40 UTC since the radar is not sensitive to fine ash (with sizes less than about 50 μm diameter) at long range, which is, indeed, dispersed in the north-east direction after the eruption ended.

Volcanic activity produces infrasonic waves (i.e., acoustic waves below 20 Hz), which can propagate in the atmosphere, useful for the remote monitoring of volcanic activity [20]. IS associated with explosive eruptions is generally produced by the rapid expansion of the gas–particle mixture within the conduit, and in consequence, it is related to the dynamics of

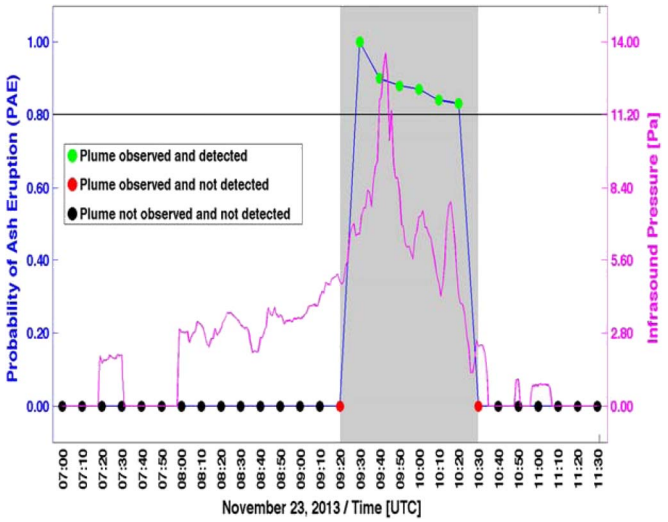

Fig. 10. Temporal sequence (blue curve) of estimated PAE, sampled every 10 min as extracted by VAD from X-band radar data, on November 23, 2013, during the Mt. Etna eruption. Gray areas mark instants where PAE was labeled "Ash," and visual inspections confirmed the presence of an ash plume. Instantaneous mean pressure from IS array (pink curve), sampled every 5 s and temporally averaged with 5-min window, is also shown.

the volume outflow and thus to the intensity of the eruption [21], [22]. At Mt. Etna, a four-element IS array (with a small aperture of 120–250 m, at an elevation of 2010 m above sea level and at a distance of 5500 m from the summit craters) has been operating since 2007 [25]. Each element has a differential pressure transducer with sensitivity of 25 mV/Pa in the frequency band 0.01–50 Hz and a noise level of 10^{-2} Pa. Array analysis is performed by a multichannel semblance grid-searching procedure using a sliding 5-s long window. The expected azimuth resolution is of $\sim 2^{\circ}$, which corresponds to about 190 m at a distance of 5.5 km. The IS array mean pressure amplitude P_{ISmean} of the acoustic signals detected by the array in 5-min long time window is usually computed for data analysis. The details on this installation, operating as part of the permanent monitoring system of Etna volcano, can be found in [25].

Similar to Fig. 7, Figs. 10 and 11 show the time series of estimated PAE and plume maximum height above the sea level, respectively, derived from the VAD algorithm during the Mt. Etna eruption of November 23, 2013. Instantaneous mean pressure from infrasonic array, sampled every 5 s, is also superimposed for the same event. The interesting feature, noted in Fig. 10, is the time shift between the MW radar detection and IS signature. In particular, in this case, the time difference between the radar-based maximum height H_M and the IS-based P_{ISmean} peak is about 17 min, the VAE-based maximum plume height above the vent is about 7.9 km, and the horizontal distance up to the H_M peak from the vent is about 12 km.

This time shift between the MW radar and P_{ISmean} IS is due to the time necessary for the plume to reach its maximum height, and therefore, it is related to the plume rising velocity. Nonetheless, while IS is peaking the increase of pressure at the vent, the radar is detecting the MW maximum values above the vent. Using data shown in Figs. 10 and 11, we can thus estimate the average uprising velocity of the erupted mixture: the vertical component is about 7.7 m/s, whereas the horizontal component is about 11.7 m/s. These estimates seem to be consistent with

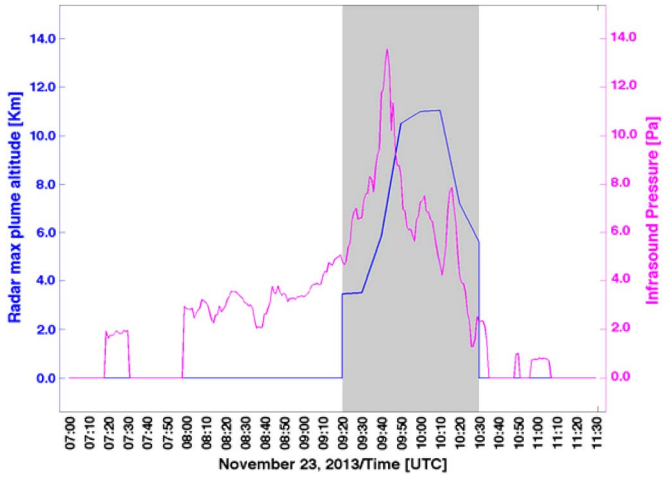

Fig. 11. Same as in Fig. 10 but for the plume maximum height above the sea level derived from VARR.

a buoyancy-driven ascent for volcanic plumes such as that on November 23. In summary, this investigation seems to confirm the following: 1) the combination of radar and IS data is an ideal ingredient for an automatic ash eruption onset early warning within a supersite integrated system (see Fig. 1), and 2) the shift between MW radar and IS array signatures may provide an estimate of the mean buoyant plume velocity field.

V. MFR Estimation at the Volcano Vent

Once the eruption onset is detected by VAD and tracked by VAT, in order to forecast the ash dispersal, it is fundamental to estimate the source MFR at the volcano vent [28]. The plume maximum height, the vertical distribution of erupted mass, and the rate of ash injection into the atmosphere all depend on the MFR, wind entrainment and advection, temperature of the erupted mixture, and atmospheric stratification [4]. In this respect, both MW radar and IS measurements can help, and in this section, we will compare them with estimates from a parametric analytical model using data of the 2010 Eyjafjallajökull, eruption [30].

During the eruption in April to May 2010 of Eyjafjallajökull stratovolcano, the ash plume was monitored by a C-band scanning weather radar, managed by the Icelandic Meteorological Office (IMO) and located in Keflavik at 155 km from the volcano [14], [15]. The single-polarization Keflavik radar provides the reflectivity factor Z_{hhm} every 5 min. By applying the VAC and VAE of the VARR algorithm (see Fig. 1), we have obtained the ash concentration estimates for each radar bin considered above the volcano vent. The trend of the plume top height shows values between 5 and 6 km above sea level in agreement with other observations [14], [15].

A. Radar-Based and Infrasonic Retrieval of Source MFR

These VAE-based ash concentration estimates have been used to provide an approximate quantification of source MFR at the vent [31]. The evolution of a turbulent plume formed above the vent during an explosive eruption can be described physically by a mass conservation equation within a volume above the vent. By integrating over the columnar volume Vc within the closed surface S_c above the vent and using the divergence theorem, we can obtain the radar-based source MFR F_{Rrad} (in

kilograms per second) defined as the sum of derivative mass rate D_R (in kilograms per second) and the mass advection rate A_R (in kilograms per second) [31]

$$F_{\mathrm{Rrad}}(t) = D_R(t) + A_R(t) \tag{11a}$$

where, if $\mathbf{r} = [x, y, z]$ is the position vector, $\mathbf{n}_0$ is the outward normal unit vector, and $\mathbf{v}_a$ is the ash mass velocity field, it holds

$$\begin{cases} D_R(t) = \iiint_{V_c} \frac{\partial C_a(\mathbf{r},t)}{\partial t} dV \\ A_R(t) = \oint_{S_c} C_a(\mathbf{r},t)\,[\mathbf{n}_0 \cdot \mathbf{v}_a(\mathbf{r},t)]\,dS \end{cases} \tag{11b}$$

where S_c is the surface enclosing the volume V_c where the mass balance is computed.

By discretizing (11), the source MFR can be estimated from weather radar measurements around the volcano vent, imposing the time step Δt equal to the radar scan sampling time (here 5 min) and setting up the horizontal section of the columnar volume V_C (here 5×5 pixels with a pixel resampled size of about 1 km per side). The 3-D vectorial velocity field $\mathbf{v}_a(\mathbf{r}, t)$ of the divergent advection rate A_R can be estimated either from radar Doppler moments (if available) or from temporal cross-correlation techniques, such as PCORR (see Section II), applied in a 3-D fashion. If the advection rate is neglected, then MFR is underestimated as advective outflow tends to remove ash from the column.

MFR can be estimated by means of infrasonic array measurements [19]–[21]. In the far-field conditions (i.e., for acoustic wavelength much larger than source dimension), the linear theory of sound demonstrates that acoustic pressure can be related to the source outflow velocity assuming a monopole, dipole, or quadrupole source of sound [34]. Thermal camera imagery suggested that the sound associated with the Eyjafjallajökull ash plume dynamics is more consistent with the dipole source [19]. Under the assumption that the acoustic velocity of the expanding surface within the conduit is equivalent to the plume exit velocity (as suggested by thermal imagery analysis of Strombolian explosions [43]), for a cylindrical conduit of radius R_v, the IS-based source MFR F_{Rifs} can be calculated as [19]

$$F_{\mathrm{Rifs}}(t) = 6.768 \cdot \rho_p \cdot R_v^{1.66} \cdot \left(P_{\mathrm{ISmean}}(t) \frac{r_s}{\rho_{\mathrm{air}}} c \right)^{\frac{1}{3}} \tag{12}$$

where R_v is the estimated radius of the vent, ρ_p is the mixture density, P_{ISmean} is the mean pressure amplitude, ρ_{air} is the density of the atmosphere, c is the sound speed, and r_s is the distance from the source (see [19] for parameter values). For this case study, the ash plume activity of Eyjafjallajökull in 2010 has been recorded using a four-element infrasonic array at a distance of 8.3 km from the craters. These sensors were chosen for their wide frequency band, good pressure sensitivity, and low power requirement (about 60 mW). All of the array elements were connected to the central station by cables, and data were digitized and transmitted via Internet link to the IMO.

B. Analytical and Model-Based Evaluation of the Source MFR

Another way to estimate MFR from the eruptive plume top height is to resort to simplified parametric empirical formulas (e.g., [4], [6], and [36]) and analytical equations (e.g., [28]). In particular, H_M can be derived from radar scans (even though the finer particles in the upper plume can be missed due to reduced sensitivity) [14], [15], [38]. The source MFR of a volcanic plume is fundamentally related to the plume top height as a result of the dynamics of buoyant plume rise in the atmosphere but is also affected by atmosphere stratification (buoyancy frequency), cross-wind, and humidity [28], [33]. A nonlinear parametric equation to estimate F_{Rmod} has been derived to include both local cross-wind and buoyancy frequency conditions at a given instant [28]

$$F_{\mathrm{Rmod}}(t) = a_0 \left[a_1 H_M^4(t) + a_2 H_M^3(t) \right] \tag{13}$$

where a_0, a_1, and a_2 are coefficients dependent on the gravitational acceleration, air and plume density, air and plume temperature, specific heat capacity of both air and particles, buoyancy frequency, radial entrainment, wind entrainment, and wind velocity profile. The application of (13) (from now on defined as D&B analytical model) at given time step t requires that the atmospheric conditions close to the volcanic vent are known in order to evaluate the plume bending under the wind effects. Under the approximation of horizontal uniformity of free troposphere, these conditions can be derived from the closest radiosounding (RaOb) station. For this case study, atmospheric conditions obtained by ECMWF ERA-40 reanalysis at 0.25° resolution interpolated above the Eyjafjallajökull volcano (see [28, Fig. S5]). The other parameters used in (13) are listed in [28, Tables S1 and S2].

The source MFR, here labeled as $F_{\mathrm{Rnum}}(t)$, can also be derived from 1-D numerical models [28]. The latter are based on the theory of turbulent gravitational convection from a maintained volcanic source taking into account wind and humidity in the atmosphere, based on Morton's theory [37]. Results from 1-D numerical models are can be obtained by Monte Carlo simulations run over a large parameter space of source conditions (temperature, exit velocity, exsolved gas mass fraction, vent radius, and vent height), atmospheric conditions (temperature, wind, and humidity profiles), and radial and wind entrainment coefficients [28]. From this ensemble of 1-D Monte Carlo simulation, minimum and maximum values of $F_{\mathrm{Rnum}}(t)$ can be derived at each time step. For these simulations, we used the same parameters and atmospheric conditions as in (13), but we also take into account the humidity atmosphere (see [28, Fig. S5]). The source conditions used can be found in [28, Table S2].

C. Intercomparison Results

The temporal trend of the VARR-based MFR $F_{\mathrm{Rrad}}(t)$ for the period of May 5–10, 2010, is shown in Fig. 12 by comparing $F_{\mathrm{Rrad}}(t)$ obtained with and without the advection term in (11) at 10-min sampling as well as every half hour, 1 h, and 3 h. The MFR variability, as detected and estimated by the weather radar, shows a pulsed behavior of the MFR at shorter time scales [31], [32]. Note that the oscillations of VARR-based MFR estimates may be affected by the time sampling of the radar and the volume scan time interval, which is accomplished in a few minutes, whereas the ash plume parameters can vary on the order of a few seconds.

Neglecting the advection term in (10) may lead to an MFR underestimation on average less than an order of magnitude or, in terms of percentage fractional difference, larger than 100% (see middle panel of Fig. 12). This VARR-derived MFR variability is about two orders of magnitudes at 10-min sampling

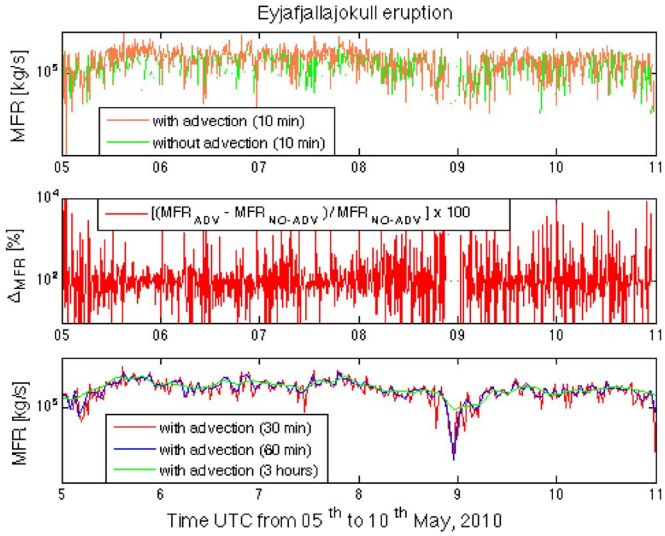

Fig. 12. (Top panel) Temporal trend of radar-derived MFR, estimated considering in (11) the A_R advection term (orange line) and without advection term (green line), within the eruption period of May 5–10, 2010. (Mid panel) Percentage fractional difference between radar-derived MFR with advection and MFR without advection term, normalized to MFR with advection. (Bottom panel) Averaged VARR-derived MFR, obtained considering the advection term, with running time windows of 30, 60, and 180 min (red, blue, and green lines, respectively).

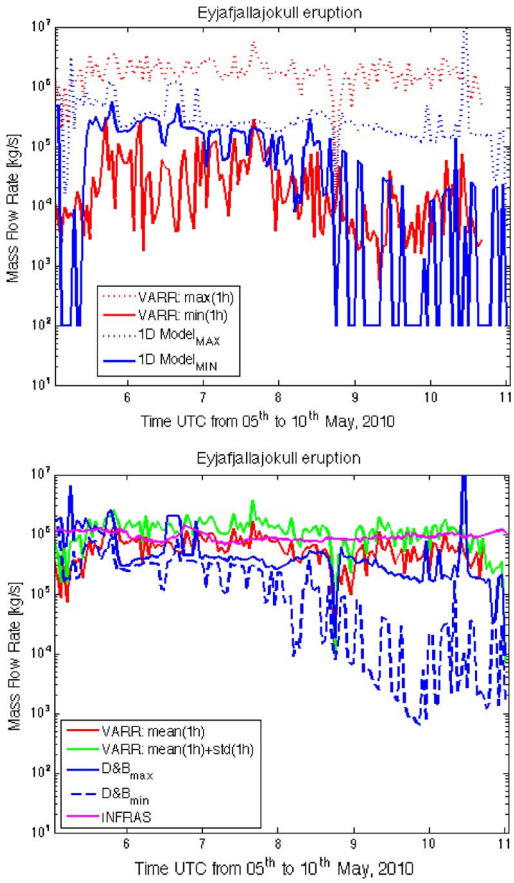

Fig. 13. (Top panel) As in Fig. 12 but showing the 1-D numerical model MFR minimum and maximum values (derived from Monte Carlo simulations using available radiosonde data) compared with the VARR-based MFR minimum and maximum values, obtained from the VARR radar algorithm within a running window of 1 h. (Bottom panel) Intercomparison among the 1-h sampled temporal trends of MFR obtained from the following: 1) VARR radar algorithm using an average of 60 min (red line) with its standard deviation (green line); 2) the D&B analytical model, applied to the minimum and maximum radar-retrieved plume heights within 1 h (blue line); and 3) IS (INFRAS) array data (pink line). See text for details.

and about an order of magnitude after 1-h averaging with a mean value around 5 10^5 kg/s within the observed period. The radar-based capability to catch the MFR intermittent behavior is, to a certain extent, expected as it closely correlates with the pulsating explosive activity through the estimate of the ash mass change and advection [32]. It is worth noting that MFR estimates from field data during the period between May 4 and 8 have provided average values between 0.6 and 2.5 10^5 kg/s [28], [30], not too far from VARR-based MFR variability around its mean value (see Fig. 12). VARR-based MFR values are also higher than those estimated by near-field video analyses between 2.2 and 3.5 10^4 kg/s [36] but closer to those derived from other plume height models between 26.2 and 43.6 10^4 kg/s [36], [33].

Fig. 13 shows the MFR temporal trends in terms of the minimum and maximum values of $F_{\mathrm{Rnum}}(t)$, derived from the Monte Carlo 1-D numerical model using radiosonde available every hour, compared to the minimum and maximum values of $F_{\mathrm{Rrad}}(t)$, derived from the VARR-based algorithm taken every 10 min within a running window of 60 min. The average value of the 1-D model MFR is about 10^5 kg/s within the observed period, whereas the minimum values are cut at 10^2 kg/s, lower values indicating that there were significant humidity effects. This only affects the minimum MFR estimate. The peak-to-peak variability of the VARR-derived estimates of MFR is typically between 10^4 and 10^6 kg/s with episodes down to 10^3 kg/s around May 9. Radar-based MFR tends to be larger than that exhibited by the 1-D numerical model, except in a few cases where the 1-D model shows much lower minimum values. These low values can be, for the most part, attributed to the strong humidity effects in the period after May 8, 2010. Due to the change in heat capacity and latent heat release associated with condensation, even plumes with very low MFRs can obtain the observed heights [28]. Additionally, there is a larger variability of the plume tops in this period, whose minimum values tend to be much lower than those before May 8.

Fig. 13 also shows the intercomparison among the 1-h sampled temporal trends of $F_{\mathrm{Rrad}}(t)$, $F_{\mathrm{Rmod}}(t)$, and $F_{\mathrm{Rifs}}(t)$, respectively, i.e., MFR estimates obtained from the VARR radar algorithm (expressed as a 1-h average together with its standard deviation), from the D&B analytical model (i.e., using (13) applied to the minimum and maximum radar-retrieved plume heights every hour; see [28] for details), from the 1-D numerical model and from infrasonic array data. Both MFR estimates of the VARR radar and IS estimates of the averaged MFR are in quite good agreement, with the IS estimate within the standard deviation of the radar-based MFR being around 10^6 kg/s. The D&B analytical model tends to provide a lower MFR especially after May 8, 2010. This behavior is strictly linked to the radar estimate of the plume top height H_M in (13), which tends to be lower in the observation period [14], [15], [29]. Indeed, radar estimates of H_M may be an underestimation of the true plume top height due to the reduced sensitivity to particle size finer than 50 μm and to the possible occlusions of observation sectors due to ground clutter.

It is also worth noting that, even at the same time sampling of 1 h, VARR-based estimates of the source MFR exhibit a higher intermittency with respect to 1-D model and IS estimates with an MFR variability larger than one order of magnitude (this variability is increased up to two orders of magnitudes at 10-min sampling in Fig. 12). This feature, which should be confirmed by future investigations, might be related to the fact that the VARR-derived MFR is strictly linked to the mass change rate and its advection, whereas 1-D model estimates depend on the plume top height (which may respond in a slower source flux changes), and IS estimates are indirectly correlated to the source MFR through the measured acoustic wave pressure. Furthermore, the uncertainty in the observed parameters of these methods is amplified by the uncertainty of the model parameters used in (12), (13), and the 1-D model. In the case of the 1-D plume model and the analytical expression (13), for example, the results can be very sensitive to the choice of entrainment coefficients [45].

VI. Conclusion

A hybrid algorithm, named VAD that exploits weather radar data, has been presented to detect the onset of the explosive volcanic eruption and estimate the MFR at the volcano vent. The VAD approach, part of the VARR methodology, can provide the PAD within the radar coverage area and the PAE at the fissure. Estimates of PAE have been provided for two eruption case studies, namely, in Iceland on 2011 and in Italy in 2013. The quantitative analysis shows very encouraging results in terms of detection and labeling which can be useful for any support decision system dealing with volcanic eruption hazard. The PAE index can be usefully exploited as a diagnostic tool for an early-warning integrated platform, which can be of interest for civil prevention and protection. Assuming to pursue a self-consistent radar approach, a way to improve PAE is to also exploit in case of uncertain labeling: 1) spatial texture of ash field radar observables versus rain field around the volcano vent; 2) temporal evolution of the radar observables around the volcano vent; 3) Doppler spectrum (mean and spectral width) variability in time and space around the volcano vent; 4) vertical section (RHI) of measured reflectivity along the radar-vent cross section; 5) detection of a strong reflectivity gradient (both in space and time) due to ash cloud; and 6) use of some polarimetric observables, such as Z_{dr}, since, for tumbling ash particles, $Z_{dr} \approx 0$ for any concentration and diameter, whereas for strong reflectivity, ash may have K_{dp} values near or less than zero as opposed to rainfall. The correlation coefficient should have low values above and around the volcano vent in case of eruption being a great mixture of nonspherical particles.

This work has also explored, using the Italian case study in 2013, the synergy between MW weather radars and infrasonic array observations. The latter have been already used for detecting Etna lava fountains with a high degree of confidence, thus demonstrating to be an essential tool for volcanic eruption early warning. Before designing an integrated tool, the interpretation of the respective signatures needs to be investigated, and this has been the goal of the presented analysis. Results indicate that the response of the weather radar and infrasonic array to the eruption onset of the plume is correlated and characterized by a time lapse due to the plume rise. The different time samplings of the two measurements, typically 10 and 1 min for radar and IS, respectively, should be taken into consideration when trying to derive eruption dynamical parameters. If confirmed by further case analyses, the synergy of weather radar and infrasonic array can be framed within the VAD hybrid algorithm by introducing a proper conditional probability of PAE driven by infrasonic array data. This may help VAD to remove ambiguous mixed-phase conditions where the ash plume is coexisting with the meteorological clouds.

Finally, VARR-based retrievals of the source MFR at the vent have been analyzed for a further event in Iceland in 2010 by comparing them with the estimates of a 1-D numerical model, an analytical formula, and infrasonic array data. The estimate of the source MFR is considered a fundamental step in characterizing the volcanic source but very difficult to measure accurately. Thus, this work for the first time has proposed the intercomparison between two experimental techniques, based on weather radar and infrasonic array data, supported by the analyses of two modeling approaches. The results show a substantial agreement about the average estimate of MFR from both instruments, with the VARR-based showing a larger variability probably due to the source pulse intermittency. The 1-D model variability is within the peak-to-peak estimate of VARR, whereas the wind-driven analytical model can underestimate MFR due to the limits in the estimation of top plume height by the radar. A 5-min time resolution appears to be a good compromise to estimate the 1-h average MFR and its standard deviation and to allow a complete volume radar scan.

Further work is required to assess the usefulness of VAD on a statistical basis using a significant number of case studies as well as to couple it with collocated infrasonic array pressure measurements. Unfortunately, only few volcanic sites are nowadays equipped with both instruments, and the historical data set is very limited so far. The PAE value and relative spatial identification by means of synergetic PAE and PAD values can be displayed continuously on a devoted web site. Positions of potentially active volcanoes should be displayed as an overlay on monitoring screens. Seismic data can complement the VARR scheme as *a priori* data in the VAD radar detection module. We expect them to be less correlated to the eruption onset, but they can corroborate and increase the VAD probability of detection. L-band Doppler radar monitoring with a fixed beam aiming near the source can be easily ingested in the detection procedure (an example can be the Voldorad L-band system near the Etna volcano). Other data, coming from ground-based and space-based remote sensors, can be also combined within VARR in order to provide a comprehensive quantitative overview of the evolving eruption scenario and its source parameters, useful for supporting the decisions of the interested Volcanic Ash Advisory Center.

Acknowledgment

The authors would like to thank B. Pálmason, H. Pétursson, and S. Karlsdóttir (IMO, Iceland) for providing the X- and C-band Iceland radar data and G. Vulpiani and P. Pagliara (DPC, Italy) for providing the X-band Italian radar data. The application of VARR chain algorithms, developed in C language and MATLAB environment, can be discussed with the authors upon request.

REFERENCES

[1] T. P. Miller and T. J. Casadevall, "Volcanic ash hazards to aviation," in *Encyclopedia of Volcanoes*, H. Sigurdsson, B. F. Houghton, S. R. McNutt, H. Rymer, and J. Stix, Eds. San Diego, CA, USA: Academic, 2000, pp. 915–930.

[2] M. O'Regan, "On the edge of chaos: European aviation and disrupted mobilities," *Mobilities*, vol. 6, no. 1, pp. 21–30, 2011.

[3] A. J. Prata and A. Tupper, "Aviation hazards from volcanoes: The state of the science," *Natural Hazards*, vol. 51, no. 2, pp. 239–244, Nov. 2009, doi: 10.1007/s11069-009-9415-y.

[4] R. S. J. Sparks *et al.*, *Volcanic Plumes*. New York, NY, USA: Wiley, 1997.

[5] A. Stohl *et al.*, "Determination of time- and height-resolved volcanic ash emissions and their use for quantitative ash dispersion modeling: The 2010 Eyjafjallajökull eruption," *Atmos. Chem. Phys.*, vol. 11, pp. 4333–4351, May 2011.

[6] L. G. Mastin *et al.*, "A multidisciplinary effort to assign realistic source parameters to models of volcanic ash-cloud transport and dispersion during eruptions," *J. Volcanol. Geothermal Res.*, vol. 186, no. 1, pp. 10–21, Sep. 2009.

[7] W. I. Rose, G. J. S. Bluth, and G. G. J. Ernst, "Integrating retrievals of volcanic cloud characteristics from satellite remote sensors: A summary," *Philos. Trans. Roy. Soc.*, vol. A358, no. 1770, pp. 1538–1606, May 2000.

[8] A. J. Prata and I. F. Grant, "Retrieval of microphysical and morphological properties of volcanic ash plumes from satellite data: Application to Mt. Ruapehu, New Zealand," *Q. J. Roy. Meteorol. Soc.*, vol. 127, no. 576, pp. 2153–2179, Jul. 2001.

[9] M. J. Pavolonis, W. F. Feltz, A. K. Heidinger, and G. M. Gallina, "A daytime complement to the reverse absorption technique for improved automated detection of volcanic ash," *J. Atmos. Ocean. Technol.*, vol. 23, no. 11, pp. 1422–1444, Nov. 2006.

[10] D. M. Harris and W. I. Rose, "Estimating particle sizes, concentrations, and total mass of ash in volcanic clouds using weather radar," *J. Geophys. Res.*, vol. 88, no. C15, pp. 10 969–10 983, Dec. 1983.

[11] C. Lacasse, S. Karlsdóttir, G. Larsen, H. Soosalu, W. I. Rose, and G. G. J. Ernst, "Weather radar observations of the Hekla 2000 eruption cloud," *Bull. Volcanol.*, vol. 66, no. 5, pp. 457–473, Jul. 2004.

[12] F. S. Marzano, E. Picciotti, G. Vulpiani, and M. Montopoli, "Inside volcanic clouds: Remote sensing of ash plumes using microwave weather radars," *Bull. Amer. Meteorol. Soc.*, vol. 94, pp. 1567–1586, Oct. 2013.

[13] F. S. Marzano, S. Barbieri, E. Picciotti, and S. Karlsdóttir, "Monitoring sub-glacial volcanic eruption using C-band radar imagery," *IEEE Trans. Geosci. Remote Sens.*, vol. 48, no. 1, pp. 403–414, Jan. 2010.

[14] F. S. Marzano, M. Lamantea, M. Montopoli, S. Di Fabio, and E. Picciotti, "The Eyjafjallajökull explosive volcanic eruption from a microwave weather radar perspective," *Atmos. Chem. Phys.*, vol. 11, pp. 9503–9518, 2011.

[15] P. Arason, G. N. Petersen, and H. Bjornsson, "Observations of the altitude of the volcanic plume during the eruption of Eyjafjallajökull, April–May 2010," *Earth Syst. Sci. Data*, vol. 3, no. 1, pp. 9–17, Sep. 2011.

[16] F. S. Marzano, S. Barbieri, G. Vulpiani, and W. I. Rose, "Volcanic ash cloud retrieval by ground-based microwave weather radar," *IEEE Trans. Geosci. Remote Sens.*, vol. 44, no. 11, pp. 3235–3246, Nov. 2006.

[17] F. S. Marzano, E. Picciotti, G. Vulpiani, and M. Montopoli, "Synthetic signatures of volcanic ash cloud particles from X-band dual-polarization radar," *IEEE Trans. Geosci. Remote Sens.*, vol. 50, no. 1, pp. 193–211, Jan. 2012.

[18] S. Scollo, M. Prestifilippo, G. Spata, M. D. Agostino, and M. Coltelli, "Monitoring and forecasting Etna volcanic plumes," *Nature Hazards Earth Syst. Sci.*, vol. 9, pp. 1573–1585, 2009.

[19] M. Ripepe, C. Bonadonna, A. Folch, D. Delle Donne, G. Lacanna, and B. Voight, "Ash-plume dynamics and eruption source parameters by infrasound and thermal imagery: The 2010 Eyjafjallajokull eruption," *Earth Planet. Sci. Lett.*, vol. 366, pp. 112–121, Mar. 2013, doi: 10.1016/j.epsl.2013.02.005.

[20] J. B. Johnson, R. C. Aster, and P. R. Kyle, "Volcanic eruptions observed with infrasound," *Geophys. Res. Lett.*, vol. 31, no. 14, Jul. 2004, Art. no. L14604.

[21] J. Caplan-Auerbach, A. Bellesiles, and J. K. Fernandes, "Estimates of eruption velocity and plume height from infrasonic recordings of the 2006 eruption of Augustine Volcano Alaska," *J. Volcanol. Geothermal Res.*, vol. 189, no. 1/2, pp. 12–18, Jan. 2010, doi: 10.1016/j.jvolgeores.2009.10.002.

[22] M. Ripepe, S. De Angelis, G. Lacanna, and B. Voight, "Observation of infrasonic and gravity waves at Soufrière Hills Volcano, Monserrat," *Geophys. Res. Lett.*, vol. 37, no. 19, Oct. 2010, Art. no. L00E14, doi: 10.1029/2010GL042557.

[23] M. Montopoli, G. Vulpiani, D. Cimini, E. Picciotti, and F. S. Marzano, "Interpretation of observed microwave signatures from ground dual polarization radar and space multi frequency radiometer for the 2011 Grímsvötn volcanic eruption," *Atmos. Meas. Tech.*, vol. 7, pp. 537–552, 2014.

[24] F. S. Marzano, M. Lamantea, M. Montopoli, B. Oddsson, and M. T. Gudmundsson, "Validating sub-glacial volcanic eruption using ground-based C-band radar imagery," *IEEE Trans. Geosci. Remote Sens.*, vol. 50, no. 4, pp. 1266–1282, Apr. 2012.

[25] G. Ulivieri, M. Ripepe, and E. Marchetti, "Infrasound reveals transition to oscillatory discharge regime during lava fountaining: Implication for early warning," *Geophys. Res. Lett.*, vol. 40, no. 12, pp. 3008–3013, Jun. 2013.

[26] S. Corradini *et al.*, "A multi-sensor approach for the volcanic ash cloud retrievals and eruption characterization," *Remote Sens.*, vol. 8, no. 1, p. 58, Jan. 2016.

[27] F. S. Marzano, M. Lamantea, M. Montopoli, M. Herzog, H. Graf, and D. Cimini, "Microwave remote sensing of the 2011 Plinian eruption of the Grímsvötn Icelandic volcano," *Remote Sens. Environ.*, vol. 129, pp. 168–184, Feb. 2013.

[28] W. Degruyter and C. Bonadonna, "Improving on mass flow rate estimates of volcanic eruptions," *Geophys. Res. Lett.*, vol. 39, no. 16, Aug. 2012, Art. no. L16308.

[29] H. Bjornsson, S. Magnusson, P. Arason, and G. N. Petersen, "Velocities in the plume of the 2010 Eyjafjallajökull eruption," *J. Geophys. Res. Atmos.*, vol. 118, no. 20, pp. 11 698–11 711, Oct. 2013, doi: 10.1002/jgrd.50876.

[30] C. Bonadonna *et al.*, "Tephra sedimentation during the 2010 Eyjafjallajokull eruption (Iceland) from deposit, radar, and satellite observations," *J. Geophys. Res.*, vol. 116, no. B12, Dec. 2011, Art. no. B12202.

[31] L. Mereu, F. S. Marzano, M. Montopoli, and C. Bonadonna, "Retrieval of tephra size spectra and mass flow rate from C-band radar during the 2010 Eyjafjallajökull eruption, Iceland," *IEEE Trans. Geosci. Remote Sens.*, vol. 53, no. 10, pp. 5644–5660, Oct. 2015.

[32] E. Kaminski, S. Tait, F. Ferrucci, M. Martet, B. Hirn, and P. Husson, "Estimation of ash injection in the atmosphere by basaltic volcanic plumes: The case of the Eyjafjallajokull 2010 eruption," *J. Geophys. Res.*, vol. 116, no. B9, Sep. 2011, Art. no. B00C02.

[33] M. J. Woodhouse, A. J. Hogg, J. C. Phillips, and R. S. J. Sparks, "Interaction between volcanic plumes and wind during the 2010 Eyjafjallajökull eruption, Iceland," *J. Geophys. Res. Solid Earth*, vol. 118, pp. 92–109, 2013.

[34] M. J. Lighthill, *Waves in Fluids*. New York, NY, USA: Cambridge Univ. Press, 1978, p. 504.

[35] D. Andronico, S. Scollo, and A. Cristaldi, "Unexpected hazards from tephra fallouts at Mt Etna: The 23 November 2013 lava fountain," *J. Volcanol. Geothermal Res.*, vol. 304, pp. 118–125, 2015.

[36] T. Dürig *et al.*, "Mass eruption rates in pulsating eruptions estimated from video analysis of the gas thrust-buoyancy transition—A case study of the 2010 eruption of Eyjafjallajökull, Iceland," *Earth, Planets Space*, vol. 67, p. 180, 2015.

[37] B. R. Morton, G. T. Taylor, and J. S. Turner, "Turbulent gravitational convection from maintained and instantaneous sources," *Proc. Roy. Soc. London, A, Math. Phys. Eng. Sci.*, vol. 234, no. 1196, pp. 1–23, Jan. 1956.

[38] B. Oddsson, M. T. Gudmundsson, G. Larsen, and S. Karlsdóttir, "Monitoring of the plume from the basaltic phreatomagmatic 2004 Grímsvötn eruption—Application of weather radar and comparison with plume models," *Bull. Volcanol.*, vol. 74, no. 6, pp. 1395–1407, 2012.

[39] A. R. Van Eaton *et al.*, "Hail formation triggers rapid ash aggregation in volcanic plumes," *Nature Commun.*, vol. 6, 2015, Art. no. 7860.

[40] G. N. Petersen, H. Bjornsson, P. Arason, and S. Von Löwis, "Two weather radar time series of the altitude of the volcanic plume during the May 2011 eruption of Grímsvötn, Iceland," *Earth Syst. Sci. Data*, vol. 4, no. 1, pp. 121–127, 2012.

[41] M. Montopoli, F. S. Marzano, E. Picciotti, and G. Vulpiani, "Spatially-adaptive advection radar technique for precipitation mosaic nowcasting," *IEEE J. Sel. Topics Appl. Remote Sens.*, vol. 3, pp. 874–884, Jun. 2012.

[42] H. Sauvageot, *Radar Meteorology*. Norwood, MA, USA: Artech House, 1992.

[43] D. DelleDonne and M. Ripepe, "High-frame rate thermal imagery of Strombolian explosion: Implication of infrasonic source dynamics," *J. Geophys. Res.*, vol. 117, no. B9, 2012, Art. no. B09206.

[44] M. Montopoli, "Velocity profiles inside volcanic clouds from three-dimension scanning microwave dual polarization Doppler radars," *J. Geophys. Res.—Atmos.*, to be published.

[45] C. Bonadonna, M. Pistolesi, R. Cioni, W. Degruyter, M. Elissondo, and V. Baumann, "Dynamics of wind-affected volcanic plumes: The example of the 2011 Cordón Caulle eruption, Chile," *J. Geophys. Res. Solid Earth*, vol. 120, pp. 2242–2261, 2015.

Frank S. Marzano (S'89–M'99–SM'03–F'15) received the Laurea degree (*cum laude*) in electrical engineering and the Ph.D. degree in applied electromagnetics from the University of Rome "La Sapienza," Rome, Italy, in 1988 and 1993, respectively.

In 1992, he was a Visiting Scientist with Florida State University, Tallahassee, FL, USA. In 1993, he collaborated with the Institute of Atmospheric Physics, National Council of Research (CNR), Rome. From 1994 to 1996, he was a Postdoctorate Researcher with the Italian Space Agency, Rome. After being a Lecturer with the University of Perugia, Perugia, Italy, in 1997, he joined the Department of Electrical Engineering, University of L'Aquila, L'Aquila, Italy, teaching courses on electromagnetic fields as an Assistant Professor. In 1999, he was a Visiting Scientist with the Naval Research Laboratory, Monterey, CA, USA. In 2002, he got the qualification to Associate Professorship and cofounded the Center of Excellence on Remote Sensing and Hydro-Meteorological Modeling (CETEMPS), L'Aquila. In 2005, he finally joined the Department of Information Engineering, Electronics and Telecommunications, Sapienza University of Rome, Rome, where he currently teaches courses on antennas, propagation, and remote sensing. Since 2007, he has been the Vice-Director of CETEMPS, University of L'Aquila, where he became the Director in 2013. He has published more than 110 papers on refereed international journals, more than 30 contributions to international book chapters, and more than 230 extended abstract on international and national congress proceedings. He was the editor of two books. His current research concerns passive and active remote sensing of the atmosphere from ground-based, airborne, and spaceborne platforms and electromagnetic propagation studies.

Dr. Marzano has been an Associate Editor of the IEEE GEOSCIENCE REMOTE SENSING LETTERS since January 2004. In 2005 and 2007, he was a Guest Coeditor of the MicroRad04 and MicroRad06 Special Issues for IEEE-GRSL. Since January 2011, he has been an Associate Editor of the journal *EGU Atmospheric Measurements Techniques*. He is a Fellow of IEEE and the Royal Meteorological Society and a member of the MWI-ICI Science Advisory Group of the EuMetSat and PMM Science Team of NASA.

Errico Picciotti received the Laurea degree (*cum laude*) in electrical engineering from the University of Ancona, Ancona, Italy, in 1993.

In 1997, he was a Radar Meteorologist with the Science and Technology Park of Abruzzo, L'Aquila, Italy. In 2002, he was a Researcher with the CETEMPS, University of L'Aquila, L'Aquila, where he worked on radar systems and polarimetry. Since 2007, he has been with HIMET, L'Aquila, where he is the Manager of the Radar Meteorology Division. His main research interests are devoted to radar meteorology and volcanic plume retrieval algorithms.

Saverio Di Fabio received the Laurea degree in electrical engineering from the University of L'Aquila, L'Aquila, Italy.

In 1998, he joined the Science and Technology Park of Abruzzo, L'Aquila, as a Microwave Engineer. From 2009 to 2012, he was a Radar Engineer with HIMET, L'Aquila. Since 2012, he has been a Senior Scientist with CETEMPS, University of L'Aquila, where he has been working on radar systems and polarimetric data processing.

Mario Montopoli received the Laurea degree in electronic engineering from the University of L'Aquila, L'Aquila, Italy, in 2004 and the Ph.D. degree in radar meteorology under a joint program from the University of Basilicata, Potenza, Italy, and Sapienza University of Rome, Rome, Italy, in 2008.

In 2005, he joined the Center of Excellence CETEMPS as a Research Scientist on ground-based radar meteorology and microwave remote sensing. In 2006, he was a Research Assistant with the Department of Electrical Engineering and Information, University of L'Aquila. From October 2011 to 2013, he was with the Department of Geography, University of Cambridge, Cambridge, U.K., under the Marie Curie FP7 European program. He is currently with the Department of Information Engineering, Sapienza University of Rome, and a EuMetSat Visiting Scientist with the H-SAF facility.

Luigi Mereu received the B.Sc. and M.Sc. degrees in telecommunication engineering from Sapienza University of Rome, Rome, Italy, in 2007 and 2012, respectively.

In 2012, he joined the Department of Information Engineering, Sapienza University of Rome, and the Centre of Excellence CETEMPS, L'Aquila, Italy, to cooperate on radar remote sensing of volcanic ash clouds within the ICT Ph.D. program. He has been involved in the FUTUREVOLC European project that started in 2012.

Mr. Mereu received the IEEE GRS South Italy Award for the Best Master's Thesis in remote sensing in 2012.

Wim Degruyter received the M.Eng.Sci. degree from the University of Ghent, Gent, Belgium, in 2006 and the Ph.D. degree in earth science from the University of Geneva, Geneva, Switzerland, in 2010.

He is currently a Senior Scientist with the Institute of Geochemistry and Petrology, Department of Earth Sciences, Zurich, Switzerland. He has been a Postdoctoral Researcher with the University of California, Berkeley, CA, USA. He was a Postdoctoral Researcher with Georgia Institute of Technology, Atlanta, GA, USA, from 2010 to 2015. His main research interests are devoted to the development of 1-D models to simulate bubble growth, magma chamber dynamics, magma ascent dynamics, and volcanic plume behavior.

Costanza Bonadonna received the B.S. degree in geology from the University of Pisa, Pisa, Italy, and the Ph.D. degree from the University of Bristol, Bristol, U.K.

She is an Associate Professor with the Department of Earth Sciences, University of Geneva, Geneva, Switzerland, and the Head of the CERG-C Program for the Assessment and Management of Geological and Climate Related Risk. She was then awarded the position of SOEST Young Investigator at the University of Hawaii, Honolulu, HI, USA, for two years and was later appointed the position of Assistant Professor at the University of South Florida, Tampa, FL, USA. She has devoted most of her research to modeling sedimentation from volcanic plumes, exploring new methodologies for the characterization of tephra-fall deposits, and developing probabilistic analyses for the assessment of tephra-fall hazards. She is now also involved in several multidisciplinary projects for the quantification of risk.

Dr. Bonadonna was a recipient of the President's Award of the Geological Society of London in 2001, the IAVCEI Outstanding Recent Graduate (George Walker Award) in 2004, the Outstanding Woman in Science Award of the Geological Society of America in 2004, and the USF Outstanding Faculty Research Achievement Award in 2005.

Maurizio Ripepe received the Laurea degree in geological sciences from the University of Florence, Florence, Italy, in 1978.

Since 1983 he has been with the Department of Earth Science, University of Florence, Florence, Italy, teaching earth physics and volcanic hazard. He was a Lecturer of geophysics and seismology with the University of Camerino, Camerino, Italy, and University of Siena, Siena, Italy (1993–2005), an External Professor with the Open University, Milton Keynes, U.K. (2001–2004), a Visiting Fellow with the University of Southern California, Los Angeles, CA, USA (1986–1989), and a Visiting Professor with the University of Hokkaido, Sapporo, Japan (2000), Ecole Normal Superioure de Physique, Lyon, France (2002), University of Tohoku, Sendai, Japan (2007), and Earthquake Research Institute, Tokyo, Japan (2009). He was also an Affiliated Researcher with the Earthquake Research Institute (ERI), Tokyo (2011). His main research interests are within geophysics and volcanology, with a focus on volcanic plumes, volcanic hazard, infrasound techniques, and field campaign activities.

Near-Real-Time Detection of Tephra Eruption Onset and Mass Flow Rate Using Microwave Weather Radar and Infrasonic Arrays

Frank S. Marzano, *Fellow, IEEE*, Errico Picciotti, Saverio Di Fabio, Mario Montopoli, Luigi Mereu, Wim Degruyter, Costanza Bonadonna, and Maurizio Ripepe

***Abstract*—During an eruptive event, the near-real-time monitoring of volcanic explosion onset and its mass flow rate (MFR) is a key factor to predict ash plume dispersion and to mitigate risk to air traffic. Microwave (MW) weather radars have proved to be a fundamental instrument to derive eruptive source parameters. We extend this capability to include an early-warning detection scheme within the overall volcanic ash radar retrieval methodology. This scheme, called the volcanic ash detection (VAD) algorithm, is based on a hybrid technique using both fuzzy logic and conditional probability. Examples of VAD applications are shown for some case studies, including the Icelandic Grímsvötn eruption in 2011, the Eyjafjallajökull eruption in 2010, and the Italian Mt. Etna volcano eruption in 2013. Estimates of the eruption onset from the radar-based VAD module are compared with infrasonic array data. One-dimensional numerical simulations and analytical model estimates of MFR are also discussed and intercompared with sensor-based retrievals. Results confirm in all cases the potential of MW weather radar for ash plume monitoring in near real time and its complementarity with infrasonic array for early-warning system design.**

***Index Terms*—Detection algorithm, microwave (MW) remote sensing, volcanic ash, weather radar.**

Manuscript received December 8, 2015; revised March 27, 2016; accepted June 3, 2016. This work was supported in part by the FUTUREVOLC Project (Grant agreement no. 308377) within the European Union's FP7/2007-2013 program. The research leading to these results has also received funding from the APhoRISM project (Grant agreement no. 606738) within FP7/2007-2013 program.

F. S. Marzano and L. Mereu are with the Dipartimento di Ingegneria dell'Informazione (DIET), Sapienza Università di Roma, 00184 Rome, Italy, and also with the CETEMPS Center of Excellence, Università dell'Aquila, 67100 L'Aquila, Italy (e-mail: marzano@diet.uniroma1.it; mereu@diet.uniroma1.it).

E. Picciotti and S. Di Fabio are with the CETEMPS Center of Excellence, Università dell'Aquila, 67100 L'Aquila, Italy, and also with HIMET Srl, 67100 L'Aquila, Italy (e-mail: errico.picciotti@himet.it; saverio.difabio@aquila.infn.it).

M. Montopoli is with the Dipartimento di Ingegneria dell'Informazione (DIET), Sapienza Università di Roma, 00184 Rome, Italy, with the CETEMPS Center of Excellence, Università dell'Aquila, 67100 L'Aquila, Italy, and also with the Institute of Atmospheric Sciences and Climate (ISAC), National Research Council (CNR), 40129 Rome, Italy (e-mail: m.montopoli@isac.cnr.it).

W. Degruyter is with the Institute of Geochemistry and Petrology, Department of Earth Sciences, ETH Zurich, 8092 Zurich, Switzerland (e-mail: wim.degruyter@erdw.ethz.ch).

C. Bonadonna is with the Department of Earth Sciences, University of Geneva, 1205 Geneva, Switzerland (e-mail: Costanza.Bonadonna@unige.ch).

M. Ripepe is with the Dipartimento di Scienze della Terra, University of Florence, 50121 Florence, Italy (e-mail: maurizio.ripepe@unifi.it).

Color versions of one or more of the figures in this paper are available online at http://ieeexplore.ieee.org.

Digital Object Identifier 10.1109/TGRS.2016.2578282

I. Introduction

DURING an explosive volcanic eruption, tephra particles are injected into the atmosphere and may severely affect air traffic and local environment, as clearly demonstrated by the Icelandic 2010 Eyjafjallajökull eruption [1]–[3]. For prevention and protection needs, a key issue is to deliver a prompt early warning of the on-going volcanic eruption and to estimate the mass flow rate (MFR) to properly initialize ash dispersion forecasting models [4]–[6]. Satellite radiometry is a well-established method for the dispersed ash plume detection and monitoring [7]. However, estimates from spaceborne visible–infrared radiometers may be limited, depending on the sensor and platform, to daylight periods, few overpasses per day, optically thin ash clouds, and, if present, obscured by water clouds [8], [9].

Complementary to satellite sensors, a ground-based microwave (MW) weather radar represents nowadays a well-established technique to monitor quantitatively a volcanic eruption and its tephra ejection [10]–[12]. Weather radars can provide a 3-D volume of eruption source parameters (e.g., plume height, particle size distribution, and MFR) as well as mass concentration and velocity fields at any time during the day or night with a periodicity of 5–15 min and a spatial resolution less than a kilometer even in the presence of water clouds [13], [14]. The major limitations of plume radar retrieval are its limited spatial coverage (e.g., less than 150 km radius around the radar site), its poor sensitivity to fine ash particles (e.g., less than a diameter of 50 μm), and the relatively long time for completing a volume scan (order of several minutes). This implies, for example, that the top of the ash column above the emission source might be only partially detected, and the extension of the horizontally spreading plume may be underestimated and tracked for a relatively short distance [15], [39].

For a quantitative estimation of ash, an algorithm, called volcanic ash radar retrieval (VARR), has been developed in the recent years using radar systems operating at S-, C-, and X-bands at single and dual polarization [16], [17]. Note that, even though the acronym VARR refers to ash estimation by MW radars, the latter are, in general, sensitive to all tephra fragments, including lapilli (2–64 mm) and blocks and bombs (>64 mm). However, the term "ash" is so widely exploited that we will use it in place of tephra, thus intending all volcanic particles injected into the atmosphere irrespective of

0196-2892 © 2016 IEEE. Personal use is permitted, but republication/redistribution requires IEEE permission.
See http://www.ieee.org/publications_standards/publications/rights/index.html for more information.

size, shape, and composition, if not otherwise specified. The VARR theoretical background, application, and validation have been extensively described in previous works [12]. One key issue, which is still open, is its extension to the detection of ash plume onset in order to be used within an early-warning system for volcanic hazard prediction. In this respect, weather radars can be complementary to the other early-warning instruments like tremor detection networks, cloud detections based on Global Positioning System receiver networks, thermal and visible cameras, and infrasonic arrays (e.g., [18], [19], and [25]). In particular, an infrasonic airwave, produced by volcanic eruptions (usually at frequencies lower than 20 Hz), can be detected as an atmospheric pressure field variation also at remote distances [20]–[22]. Arrays of infrasonic sensors, deployed as small aperture ($\sim$100 m) antennas and distributed at various azimuths around a volcano, show a tremendous potential for enhanced event detection and localization. At short distances (<10 km) from the source, the almost constant velocity of sound makes precise localization (within a few tens of meters of accuracy) possible. With respect to other systems, infrasound (IS) is also largely unaffected by cloud cover and does not rely on line-of-sight view of vents (e.g., [19] and [25]), as is the case with satellite or radar observations.

The goal of this work is to extend VARR by including a volcanic ash detection (VAD) module and designing an overall scheme for ash plume monitoring in near real time providing eruption onset time, plume tracking, and geophysical products. The focus is on the methodological issues more than its statistical validation so that examples of VAD application are shown for specific test cases. Using data from recent volcanic eruptions, time series of infrasonic array and radar acquisitions in the proximity of the volcanic vent are used together to understand the potentiality of combining the two ground-based measurements for eruption onset early warning. Detection and estimation of MFR are also evaluated and compared with estimates from analytical equations, 1-D volcanic plume models, and IS-based methods.

The basic idea of VAD is that, during standard operations, the radar algorithm is set into a "meteorological mode" (devoted to monitoring precipitating water cloud echoes), but a special processing is envisaged at the locations where potentially active volcanoes are present within the radar coverage area. VAD continually runs for each radar volume acquisition. Whenever the VAD detection test is passed (i.e., an eruption is confirmed from VAD radar data analysis), the VARR data processing switches into an "ash mode," and the tracking module is activated (manually or automatically depending on the system). Note that near-real-time tracking of volcanic cloud dispersal represents an essential datum both for aviation and civil safety. Early-warning advisory can be spread to the local authorities if the ash plume trajectory threatens some sensitive areas (e.g., airports, aviation routes, critical infrastructures, towns, and metropolitan regions). In addition, the indication of the velocity of the transported plume provided by the tracking module can be a useful and alternative way for the retrieval of the plume altitude given the knowledge of the velocity–altitude profile obtained, for example, by radiosoundings and/or meteorological forecasts.

This paper is organized as follows. Section II will provide an overview of VARR block diagram, including the VAD module. The latter will be described in detail using a hybrid fuzzy logic and conditional probability approach. By exploiting available data, Sections III and IV will show examples of VAD applications for the Icelandic Grímsvötn eruption that occurred in 2011 and the Italian Mt. Etna volcano eruption that occurred in 2013. In the latter event, radar-based retrievals will be compared with infrasonic array data to interpret the respective signatures and explore their synergy. In Section V, VARR-based retrievals of the MFR at the vent will be analyzed for the May 5–10 period of the 2010 Eyjafjallajökull eruption by comparing them with estimates from the 1-D numerical model, analytical formula, and infrasonic array. Section VI will draw the conclusion and future work recommendations.

II. Designing VARR

The objective of this section is to illustrate an overall algorithm for MW weather radar polarimetric retrieval of volcanic ash plumes, including four major stages: detection, tracking, classification, and estimation of ash (i.e., in our context, all volcanic particles injected into the atmosphere irrespective of size, shape, and composition). The underlying concepts will be illustrated by sketching the underpinning philosophy and the basic theory, referring to previous works where possible for the discussion of tracking, classification, and estimation modules [12]. Only the detection module will be described in detail in Section II-B since it is the innovative module of this work.

The basic assumption in this work is that, in a given radar site, we have at disposal a set of variables at a specific frequency band (e.g., S-, C-, and X-bands) at single or dual polarization with a given range, azimuth, and elevation resolution (e.g., 250 m, 1°, and 1°, respectively). The latter defines the so-called radar resolution bin, and for each bin, we can introduce a polarimetric radar observable vector $\mathbf{z}_m = [Z_{hhm}, Z_{drm}, K_{dpm}, \rho_{hv}, L_{drm}]$, where Z_{hhm} is the measured copolar reflectivity factor, Z_{drm} is the differential reflectivity, K_{dpm} is the differential phase shift, ρ_{hv} is the copolar correlation (modulus) coefficient, and L_{drm} is the linear depolarization ratio. Since the availability of all of these observables is not always guaranteed, depending on the system capability, some of them can be discarded from the analysis, thus impacting the estimation accuracy. Details on the exploitation of dual-polarization and single-polarization radar systems can be found in [17] and [23]. All modules of VARR are supposed to operate on a volume-bin basis, whereas the use of spatial texture processing is foreseen but not discussed here.

A. Overall VARR Scheme

The VARR algorithm for polarimetric MW radars is, in a very general context, structured in the following four main modules, shown in Fig. 1.

1) VAD is detecting the ash plume onset from measured $\mathbf{z}_m$. The VAD algorithm is mainly devoted to characterizing the typical ash radar signature, possibly separating the

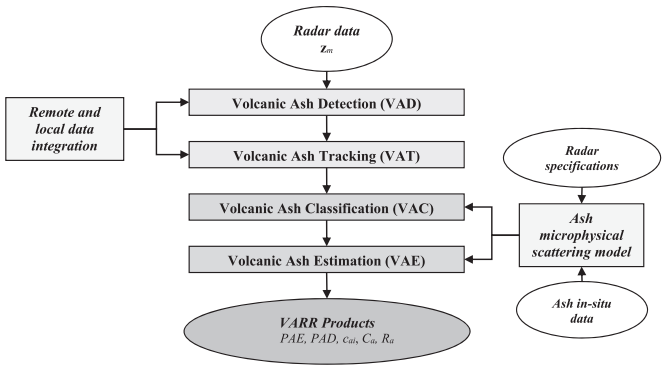

Fig. 1. At each time step and for each radar bin, VARR can provide probability of ash eruption PAE (in percent) and detection PAD (in percent), ash classification c_{ai} [i.e., mean particle diameter D_n (in millimeters)], ash mass concentration C_a (in grams per cubic meter), and ash fall rate R_a (in kilograms per square meter second). If Doppler capability is present, ash mean velocity v_{ma} (in meters per second) and ash velocity standard deviation σ_{va} (in meters per second) can be also estimated. Moreover, some other useful products could be derived, such as ash plume top height H_M (in meters), ash erupted volume V_a (in cubic meter), ash mass loading L_a (in kilograms per square meter), and ash MFR F_{Ra} (in kilograms per second).

radar bins affected by ash from those mainly interested by meteorological targets.

2) *Volcanic ash tracking* (VAT) is tracking the ash plume dispersion from measured $\mathbf{z}_m$ within the radar coverage area. The VAT algorithms are the basis of monitoring and nowcasting the displacement of the ash mass in space and time.
3) *Volcanic ash classification* (VAC) is classifying ash particle class from measured $\mathbf{z}_m$ within each radar bin in terms of particle's size, shape, and orientation. The VAC module is based on the maximum *a posteriori* probability (MAP) criterion trained by a forward particle MW scattering model.
4) *Volcanic ash estimation* (VAE) is estimating the ash concentration, fall rate, ash mean diameter, and other volcanic products from the measured $\mathbf{z}_m$ within each radar resolution bin.

Fig. 1 shows a flowchart of the VARR scheme. The VAD and VAT modules can be supported by the integration of other available measurements, e.g., remote sensing data from spaceborne infrared radiometers, ground-based infrasonic arrays, and lidars or *in situ* data, such as ash disdrometers or human inspections. On the other hand, the VAC and VAE modules are fed by the forward microphysical-electromagnetic scattering models ingesting information about weather radar instrumental characteristics and possible *in situ* sampling of previous eruptions.

The VAD module will be described in the next section, being the main objective of this work.

The VAT module takes as input the detection of the ash plume target and tracks it in time and space. In order to accomplish this task, a phase-based correlation technique (PCORR), well described in [24] and here only summarized, is used for this purpose. In order to estimate the displacement field, the PCORR algorithm exploits the comparison between two consecutive radar images, typically the constant altitude plan position indicator (PPI) but applicable to any radar observed or estimated field $F_{\rm rad}$. The displacement field is expressed by the horizontal motion vector $\mathbf{V}(x, y)$ for each position (x, y) in the horizontal plane and whose Cartesian components $u(x, y)$ and $v(x, y)$ are used within an advection scheme to forecast the next radar image [24], [41]

$$\hat{F}_{\rm rad}(x, y, t + n\Delta t) = F_{\rm rad}(x - u \cdot n\Delta t, y - v \cdot n\Delta t, t) \quad (1)$$

where t is the current time, Δt is the time step of radar acquisition (e.g., 5, 10, or 15 min), and $n\Delta t$ is the lead time with respect to current time (e.g., 30 or 60 min in advance). The estimate of u and v components is carried out by computing the normalized Fourier transform of the spatial cross-correlation function $S_{Fcx}(\Delta x, \Delta y)$ and by extracting the spatial shift $(\Delta x, \Delta y)$ from the phase component of S_{Fcx}.

The frequency-domain approach improves the accuracy of motion directions and magnitude estimates by avoiding saturation effects in proximity of the correlation function multiple maxima. The limitations of PCORR, applied as described, are the following: 1) when applied to the whole radar image, it can provide only one motion vector per image, thus implicitly supposing a steady-state field, and 2) sources and sinks of radar observables are not considered so that the field is displaced but not modified in its value. These issues can be partially addressed by resorting to a spatially adaptive segmentation of the observed radar field to generate a spatially variable advection field. This approach can forecast the rotation and deformation of the observed field and has been successfully applied to atmospheric precipitation on a relatively large scale, even though physical models of sources and sinks are not taken into account [41]. By comparing the nowcasted and actual reflectivity maps, the accuracy of the predicted field decreases, as expected, with the increase of the lead time $n\Delta t$; percentage errors of 75% can be typically obtained at 0.5 h and of 60% at 1 h, but a detailed analysis is beyond the scopes of this work.

The VAC module is widely described in [16] and [17] and here only summarized. Ash category classification is carried out by applying the Bayesian theory in a supervised manner, i.e., we evaluate the posterior probability density function (pdf) by using the forward microphysical scattering model [16], [12]. When maximizing the posterior pdf, the method is called MAP, and the estimated ash class c_a at each time step and radar bin is expressed by [16]

$$\begin{aligned}\hat{c}_a &= \text{Mode}_c \left\{ p(c_a | \boldsymbol{z}_m) \right\} \\ &= \text{Mode}_c \left\{ p(\boldsymbol{z}_m | c_a) p(c_a) / p(\boldsymbol{z}_m) \right\} \end{aligned} \quad (2)$$

where p represents the pdfs, Mode_c is the modal operator, and $\mathbf{z}_m$ is the polarimetric radar observable vector, with $p(c_a|\boldsymbol{z}_m)$, $p(\boldsymbol{z}_m|c_a)$, and $p(c_a)$ being the posterior, likelihood, and *a priori* pdfs, respectively. The ash class c_a is usually provided in terms of size (i.e., fine ash: < 63 μm, coarse ash: 63 μm–2 mm, and lapilli: 2–64 mm together with blocks and bombs larger than 64 mm) and mass concentration category (e.g., low: average around 0.1 g/m^3, medium: average around 1 g/m^3, and high: average around 5 g/m^3). The *a priori* pdf $p(c_a)$ is used to insert available information on the requirements that make the existence of the class c_a likely in a given environmental condition. The *a priori* pdf is typically set uniform unless there

is evidence of prevailing ash class. A usual simplifying assumption of MAP is to introduce a multidimensional Gaussian pdf model in order to reduce (2) to the minimization of quadratic metrics, i.e., the squared generalized distance between the available polarimetric measurement and the corresponding class centroids, obtained from the forward microphysical scattering model [16]. The advantage of a supervised Bayesian approach is the flexibility and rigorousness to deal with all data, but on the other hand, it strongly relies on the accuracy of the forward training model.

The VAE module is well described in [12], [16], and [17] so that here it is only summarized. The Bayesian approach can be also used, in principle, for the estimation of physical source parameters. In case we are able to assume a function model f_{est} to relate the predicted parameter with available measurements, then the Bayesian method reduces to statistical regression so that the estimated volcanic ash parameter P_a is expressed by [17]

$$\hat{P}_a = f_{\text{est}}(\boldsymbol{z}_m; \boldsymbol{r}|\hat{c}_a) \tag{3}$$

where $\boldsymbol{r}$ is the vector of unknown regression coefficients which are found by a minimum least square technique, conditioned to estimated ash category c_a. The latter is again found by resorting to the forward training model with all potential and limitations discussed for VAC. The choice of the functional relationship may be critical, but on the other hand, it greatly simplifies the estimation step and makes it computationally very efficient. A power-law regression model can be chosen for ash mass concentration and fall rate for (3) [16], [17]. As listed in Fig. 1, at each time step and for each radar bin, VAE can provide ash mass concentration C_a (in grams per cubic meter), ash fall rate R_a (in kilograms per square meter second), and mean particle diameter D_n (in millimeters). If Doppler capability is present and proper algorithms are applied such velocity-azimuth display [42], ash mean velocity v_{ma} (in meters per second) and ash velocity standard deviation σ_{va} (in meters per second) in both horizontal and vertical directions can also be estimated [44]. Moreover, some other products can be derived from the overall volume analysis at each time step, such as ash plume top height H_M (in meters), ash plume volume V_a (in cubic meters), ash mass loading L_a (in kilograms per square meter), and ash MFR F_{Ra} (in kilograms per second). The latter is described in Section V-A.

B. VAD Module

Detection of ash clouds is a cumbersome problem as their signature can be confused, from an MW radar point of view, with hydrometeor features. In this paragraph, a methodology is presented for the real-time automated identification of volcanic solid particle emissions, based on the availability of weather radar data every Δt minutes. The detection (or monitoring) method here discussed exploits the analysis of copolar reflectivity measurements associated to geographical digital information. This is justified by the fact that most operational radar systems are single polarization only so that this choice implies the applicability of our VAD methodology to all weather radars currently used for volcano monitoring. Its generalization to polarimetric radar data is beyond the scopes of this work, but it is, of course, feasible [17]. The proposed scheme for monitoring and tracking ash plumes is presented in Fig. 2.

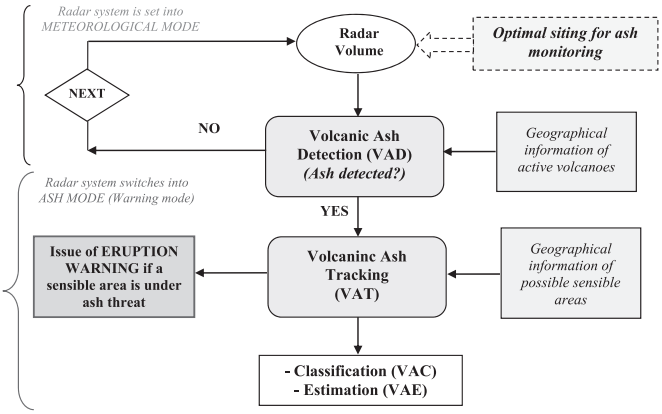

Fig. 2. Schematic block diagram for ash detection (VAD) coupled with tracking (VAT), classification (VAC), and estimation (VAE) modules. Radar 3-D volumes are available typically every 5, 10, or 15 min, depending on the range-elevation-azimuth scanning schedule and system specifications.

As described in Section II-A, weather radar data can be integrated with information received from different available sources, such as remote sensors from ground stations, space platform, and the Volcanic Aviation Advisory Center bulletin. The efficacy of radar detection and tracking of ash plumes is, of course, conditioned by the optimal choice of radar site, which may limit the volcanic vent MW visibility.

The VAD algorithm is designed for the following: 1) to keep pace with real-time data and to provide a detection result at the end of each radar volume acquisition (as fast as possible in order to follow the eruption dynamics) and 2) to store previous acquired data (at least 1 h), to be maintained in a database in order to allow further analyses if needed. Radar algorithms can usually be applied to measurements represented in native spherical coordinates or to data in resampled Cartesian coordinates, which allows a simpler geometrical interpretation. The VAD algorithm, instead of using the radar 3-D volume, is applied to a bidimensional (2-D) product, such as the vertical maximum intensity (VMI) which is the maximum value of measured reflectivity along the column at each Cartesian ground pixel (x, y) or $(i.j)$ in its discrete form. The advantage of considering VMI is the reduction of the processing complexity, making VAD computationally more efficient. In addition, since VMI privileges the reflectivity peaks that are present in a radar volume, it results more suitable for hazard warning. Obviously, all noise contaminations in radar volumes (e.g., ground clutter, second trip echoes, and anomalous propagation effects) must be filtered out in order to efficiently discriminate atmospheric targets. The VAD technique should use the appropriate scan strategy (i.e., the number of elevation-azimuth angles) that is a critical decision during operational use. The choice shall depend on the distance between the volcano and the radar and on the heights of radar beams with respect to the surface.

The VAD algorithm starts splitting the coverage area, where all potentially active volcano vents are located, in three (or more) concentric circular sectors arbitrarily centered on the volcano location. As an example, Fig. 3 shows how the sectors are subdivided for the Mt. Etna (left panel) and the Grímsvötn

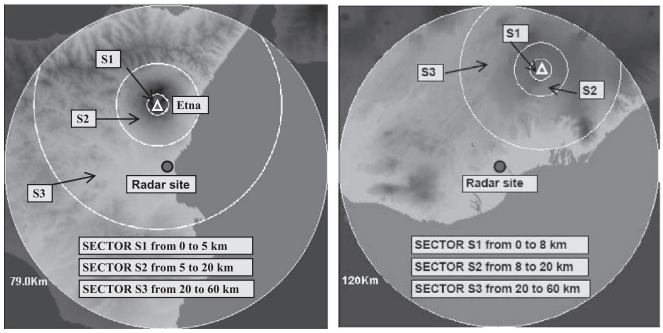

Fig. 3. Three sectors in which the Mt. Etna volcanic area (left panel) and Grímsvötn volcanic area (right panel) are subdivided. Circular sectors s_1, s_2, and s_3 have different radii in the two areas due to different setups, and within each of them, radar observables are processed by the VAD algorithm.

volcanic target area (right panel). Due to the diverse geographical characteristics and radar installations, the homologous sectors have different sizes in the two analyzed target areas. The basic idea is to mark each concentric circular sector s_k (e.g., $k = 1, 2, 3$) with the class labels $s_k =$ yes (Y) or $s_k =$ no (N), according to a hybrid fuzzy logic probabilistic strategy.

The block diagram of the VAD algorithm is structured along the following steps.

1) Define concentric circular sectors s_k of diameters $d_1 < \cdots < d_k < d_{k+1}$ within the radar maximum coverage area and centered on the volcano vent (typically $k = 3$).
2) Extract within these sectors s_k and at each discrete time step t_n the following features at each pixel $(i.j)$: a) the reflectivity VMI values $Z_M(s_k, i, j, t_n)$; b) the echo-top height values $H_M(s_k, i, j, t_n)$, which are the maximum height values where $Z_M(s_k, i, j, t_n) > S_{Zk}$ and where S_{Zk} is a proper threshold that is empirically derived; and c) the percentage $N_p(s_k, t_n)$ of N_k pixels of Z_M above the threshold signal S_{Zk} with respect to the total sector pixels $N_{\rm tot}(s_k)$ so that $N_p(s_k, t_n) = 100\ N_k/N_{\rm tot}(s_k)$, with N_k larger than a threshold signal S_{Zk}. This threshold is empirically set and may be site dependent (e.g., see Section III and Table I).
3) Convert each feature X (with $X = Z_M$, H_M, or N_p) into a membership probability using a ramp membership function $M_X[X; X_{\rm th}, \Delta X]$. The latter is defined as a function of the threshold parameter $X_{\rm th}$ and interval parameter ΔX so that

$$\begin{cases} M_X[X; X_{\rm th}, \Delta X] = 0 \text{ if } X < X_{\rm th} \\ M_X[X; X_{\rm th}, \Delta X] = 1 \text{ if } X > X_{\rm th} + \Delta X \\ M_X[X; X_{\rm th}, \Delta X] = \Delta X^{-1}(X - X_{\rm th}) \text{ elsewhere.} \end{cases} \tag{4}$$

The values of the thresholds and interval parameters depend on the radar scan strategy, distance volcano–radar, and their relative altitude, radar azimuth, and range resolution and circular sector topology (e.g., see Section III and Table I).
4) Define an inference rule function for each sector s_k as the product of the membership function of each feature X (*fuzzification stage*)

$$I_k[Z_M, H_M, N_p; s_k] = M_Z[Z_M] M_H[H_M] M_N[N_p]. \tag{5}$$

5) Assign a label "Y" (yes) or "N" (no) to each sector s_k at each time step t_n, taking the maximum of the inference rule function I_k and checking if it is greater or lesser than 0.5 (*defuzzification stage*)

$$\text{Max}_{i,j}\left\{I_k[Z_M, H_M, N_p; s_k]\right\} = \begin{cases} \geq 0,5 & \rightarrow\ S_k = Y \\ < 0,5 & \rightarrow\ S_k = N \end{cases} \tag{6}$$

where the maximum Max_{ij} is searched within all pixels (i, j) of sector k if the percentage number of pixels is above a given threshold S_{Nk} that is typically empirically derived.
6) Estimate a probability of ash eruption (PAE) at a given time step t_n by evaluating different temporal combinations for $s_k = Y$ or N at previous time steps t_{n-i} (with $i = 1 \div N_V$) as follows (*ash eruption conditional probability stage*):

$$\text{PAE}(t_n) = p_{\rm ash}(t_n, s_1 | s_2, s_3) p_{\rm avg}(\Delta t_n, s_1 | s_2, s_3) \tag{7a}$$

with

$$\begin{aligned} & p_{\rm ash}(t_n, s_1 = Y | s_2, s_3) > 0 \\ & p_{\rm avg}(\Delta t_n, s_1 = Y | s_2, s_3) = \frac{1}{N_V} \sum_{i=1}^{N_V} p_{\rm ash}(t_{n-i}, s_1 | s_2, s_3) \\ & p_{\rm ash}(t_n, s_1 = N | s_2, s_3) = 0 \end{aligned} \tag{7b}$$

where $p_{\rm ash}(t_n, s_1 = Y | s_2, s_3)$ and $p_{\rm ash}(t_{n-i}, s_1 | s_2, s_3)$ are the ash conditional probabilities, respectively, at present instant t_n and at previous acquisition time steps t_{n-i} for a given class label combination in s_1, s_2, and s_3, whereas N_V is the number of volumes considered in previous acquisition time steps within the interval Δt_n. PAE in (7) is the product of two conditional probabilities of ash: the current probability of ash when in the inner sector $s_1 = Y$ and the temporal average of past probabilities in sector s_1, both conditioned to the outcomes of (5) in outer sectors s_2 and s_3. Note that the PAE value is computed automatically after every radar volume scan, and its value ranges from 0 to 1.

The time span Δt_n of the average probability $p_{\rm avg}$ is typically set to 1 h so that $N_V = \Delta t_n / \Delta t$, with Δt as the time step of radar acquisition. Both $p_{\rm ash}(t_n)$ and $p_{\rm ash}(t_{n-i})$ are empirically tunable probabilities, depending on the volcanic observation scenario and available information. These conditional probabilities are meant to discriminate ash plumes from meteorological storms, exploiting their different temporal evolutions. As an example, from the analysis of past case studies of volcanic eruptions in Iceland and Italy, Tables II and III provide, respectively, the conditional current and previous probability $p_{\rm ash}$ in (7), derived from label combinations in sectors 2 and 3 and depending on the label (Y or N) of sector 1. It is worth recalling that, if $s_1 = N$ at current instant t_n, the PAE value is set to zero automatically. The proposed values in the previous tables basically guarantee that volcanic ash is not detected in cases of persistent and/or widespread radar echoes, likely due to moving stratiform

TABLE I
PARAMETERS OF THE VAD MEMBERSHIP FUNCTIONS M_X, AS DESCRIBED IN (4), IN THE THREE SECTORS FOR THE 2011 GRÍMSVÖTN CASE STUDY

Symbol	Parameter	Units	Value in sector s_1 (k=1)	Value in sector s_2 (k=2)	Value in sector s_3 (k=3)
Z_{Mth}	VMI reflectivity	dBZ	20	20	15
ΔZ_M	VMI reflectivity interval	dBZ	10	10	10
H_{Mth}	Max altitude	km	0.8	1.4	1.4
ΔH_M	Max altitude interval	km	1	0.6	0.6
N_{pth}	Percentage pixel number threshold	%.	0	0	0
ΔN_p	Percentage pixel number interval	%.	100	40	10
S_{Zk}	VMI reflectivity threshold	dBZ	20	15	10
S_{Nk}	Pixel number threshold	Adim.	3	8	100
$N_{tot(Sk)}$	Total pixel number	Adim.	5021	26392	216384

TABLE II
CONDITIONAL PROBABILITY p_{ash} FOR SECTORS 2 AND 3 ONCE SECTOR 1 IS MARKED AS Y ($s_1 = Y$) AT PRESENT INSTANT t_n OR AT PREVIOUS INSTANTS t_{n-i}. NOTE THAT, IF $s_1 = N$ AT CURRENT INSTANT t_n, THE PAE VALUE IS SET TO ZERO AUTOMATICALLY. THE RATIONALE BEHIND IS THAT VOLCANIC ASH IS NOT DETECTED IN CASES OF PERSISTENT AND/OR WIDESPREAD RADAR ECHOES DUE TO METEOROLOGICAL CLOUDS

Label combination if s_1=Y	**Sector 3** labeled as s_3=**Y**	**Sector 3** labeled as s_3=**N**
Sector 2 labeled as s_2=**Y**	$p_{ash}(t_n, s_1=\mathrm{Y} \mid s_2=\mathrm{Y}, s_3=\mathrm{Y}) = 0.00$	$p_{ash}(t_n, s_1=\mathrm{Y} \mid s_2=\mathrm{Y}, s_3=\mathrm{N}) = 0.50$
Sector 2 labeled as s_2=**N**	$p_{ash}(t_n, s_1=\mathrm{Y} \mid s_2=\mathrm{N}, s_3=\mathrm{Y}) = 0.70$	$p_{ash}(t_n, s_1=\mathrm{Y} \mid s_2=\mathrm{N}, s_3=\mathrm{N}) = 1.00$

TABLE III
CONDITIONAL PROBABILITY p_{ash} FOR SECTORS 2 AND 3 ONCE SECTOR 1 IS MARKED AS N ($s_1 = N$) AT PREVIOUS INSTANTS t_{n-i}

Label combination if s_1=N	**Sector 3** labeled as s_3=**Y**	**Sector 3** labeled as s_3=**N**
Sector 2 labeled as s_2=**Y**	$p_{ash}(t_{n-i}, s_1=\mathrm{N} \mid s_2=\mathrm{Y}, s_3=\mathrm{Y}) = 0.00$	$p_{ash}(t_{n-i}, s_1=\mathrm{N} \mid s_2=\mathrm{Y}, s_3=\mathrm{N}) = 0.75$
Sector 2 labeled as s_2=**N**	$p_{ash}(t_{n-i}, s_1=\mathrm{N} \mid s_2=\mathrm{N}, s_3=\mathrm{Y}) = 0.65$	$p_{ash}(t_{n-i}, s_1=\mathrm{N} \mid s_2=\mathrm{N}, s_3=\mathrm{N}) = 1.00$

meteorological storms covering the outer sectors in the volcano surrounding. Convective rain clouds, developing close to the volcano vent as in many tropical volcanoes, might be confused with ash plumes. In this respect, radar polarimetry could help in refining the detection procedure. From our experience, for the Icelandic and Italian volcanic eruption cases, PAE ≥ 0.8 is associated to the presence of ash plumes, whereas PAE ≤ 0.6 is mainly due to meteorological targets. On this basis, as soon as sector 1 is labeled as Y, the PAE value is computed by means of (7).

7) Label the radar echoes around the potential volcanic vent in the inner sector s_1 at instant t_n by means of $L_{\mathrm{PAE}}(t_n, s_1)$, defined as (*ash eruption target labeling stage*)

$$L_{\mathrm{PAE}}(t_n, s_1) = \begin{cases} \text{Meteorological} & \text{if } 0 \leq \mathrm{PAE} < T_{E1} \\ \text{Uncertain} & \text{if } T_{E1} \leq \mathrm{PAE} < T_{E2} \\ \text{Ash} & \text{if } \mathrm{PAE} \geq T_{E2} \end{cases} \tag{8}$$

where T_{E1} and T_{E2} are proper thresholds, typically set to 0.6 and 0.8, respectively, as mentioned before.

8) The spatial identification of radar echoes, affected by ash, can be performed by introducing the probability of ash detection (PAD). The latter is an areal probability of detection applied to all pixels within the radar coverage estimated as (*ash detection conditional probability stage*)

$$\begin{aligned} \mathrm{PAD}(i, j, t_n) = \{ & w_z M_z \left[Z(i, j) \right] \\ & + W_H M_H \left[H_M(i, j) \right] \} M_D \left[d(i, j) \right] \end{aligned} \tag{9}$$

where the new membership function MD takes into account the distance between the pixel (i, j) and the volcano vent. Roughly speaking, (9) reveals the presence of ash in a given pixel if there is a suitable distance from the vent via d, if those pixels lie in a specified range of altitudes via H_M, and if the maximum reflectivity is sufficiently high via Z_M. PAD values are in the same range of the PAE; in (9), the weights w_z and w_H can be set to 0.5, but they can take into account the instantaneous availability of each source of information and its strength. The PAD formula in (9) may be enriched and improved by exploiting additional radar features, such as spatial texture and gradient of reflectivity, radial velocity, and some polarimetric features.

9) In similar fashion to (8), we can then define a radar detection label $L_{\mathrm{PAD}}(t_n, i, j)$, which has generally different thresholds T_{E3} and T_{E4}. The L_{PAD} label is introduced to discriminate among meteorological and ash in each pixel of the radar domain, taking into account any uncertain or mixed condition (*ash detection target labeling stage*)

$$L_{\mathrm{PAD}}(t_n, i, j) = \begin{cases} \text{Meteorological} & \text{if } 0 \leq \mathrm{PAD} < T_{E3} \\ \text{Uncertain} & \text{if } T_{E3} \leq \mathrm{PAD} < T_{E4} \\ \text{Ash} & \text{if } \mathrm{PAD} \geq T_{E4}. \end{cases} \tag{10}$$

If $L_{\mathrm{PAE}}(t_n, s_1) = \text{Ash}$, the VAD algorithm switches (automatically or semiautomatically) into a warning mode so that tracking (VAT), classification (VAC), and estimation (VAE) procedures can be activated. These modules are applied to (i, j) pixels, where $\mathrm{PAD}_k(i, j, t_n) \geq T_{E3}$, in order to keep pixels labeled as ash or as uncertain. The probability PAE

TABLE IV
CONDITIONAL PROBABILITY $p_{\rm ash}$ FOR SECTORS 2 AND 3 IF SECTOR 1 IS MARKED $s_1 = Y$ AT CURRENT AND PREVIOUS INSTANTS t_{n-i} AND IF PAE ≥ 0.80 (ASH ECHO)

Label combination if s_1=YES and PAE(t_{n-1}) seems to confirm an eruption	**Sector 3** labeled as s_3=**Y**	**Sector 3** labeled as s_3=**N**
Sector 2 labeled as s_2=**Y**	$p_{ash}(t_n,s_1=\text{Y}\|s_2=\text{Y},s_3=\text{Y})=0.4$	$p_{ash}(t_n,s_1=\text{Y}\|s_2=\text{Y},s_3=\text{N})=0.9$
Sector 2 labeled as s_2=**N**	$p_{ash}(t_n,s_1=\text{Y}\|s_2=\text{N},s_3=\text{Y})=0.75$	$p_{ash}(t_n,s_1=\text{Y}\|s_2=\text{N},s_3=\text{N})=1$

in (7), immediately after the ash detection instant t_n, must be evaluated with Table IV, instead of Table II, in order to verify if the volcanic ash eruption from the vent is a continuing phenomenon.

If $L_{\rm PAE}(t_n, s_1) =$ Uncertain, reflectivity echoes can be affected by false alarm or misdetection due to mixed phase (hydrometeor and ash signatures) or under particular atmospheric conditions.

If $L_{\rm PAE}(t_n, s_1) =$ Meteorological, VARR chain successive modules are not activated, and the detection cycle is updated to the next time step. Note that, if immediately after $L_{\rm PAE}(t_n, s_1) =$ Ash, then $s_1 = N$, PAE is set to zero, and probably a false alarm may have happened or it may behave intermittently. On the other hand, if the eruption stops after some time, dispersed ash will be detected only into outer sectors but not in the inner sector s_1. In these cases, VAT, VAC, and VAE are applied anyway to (i, j) pixels, where PAD$(i, j, t_n) \geq T_{E3}$.

In summary, the probability of the volcanic eruption onset is described in time by the PAE time series evolution. Its behavior is an indicator of eruption column ejecting ash in the surrounding of the volcanic vent. On the other hand, the spatial discrimination between ash and meteorological radar echoes is performed by PAD maps. The efficiency of the latter is, of course, essential for any prompt and effective support to decision.

III. RADAR-BASED DETECTION OF VOLCANIC ERUPTION ONSET

The VAD algorithm has been tested for several volcanic eruptions and requires that a weather radar is available and operating during the eruption, which is not always the case when eruptions occur.

As an example, here we will show the results obtained from the volcanic eruption that occurred in May 2011 at the Grímsvötn volcano, located at the northwest of the Vatnajökull glacier in south-east Iceland (e.g., [27]). It is one of the most active Icelandic volcanoes. An explosive subglacial volcanic eruption started in the Grímsvötn caldera around 19:00 UTC on May 21, 2011. The strength of the eruption decreased rapidly, and the plume was below ~10-km altitude after 24 h [40]. The eruption was officially declared over on May 28 at 07:00 UTC. More details on the Grímsvötn eruption observations and estimates can be found in [27] and [23] with a comprehensive analysis of the eruptive event from VAC and VAE results using polarimetric radar data at X-band.

The X-band dual polarization radar measurements (DPX) used in this study are acquired by the Meteor 50DX system which is a mobile compact weather radar deployed on a transportable trailer. For the volcanic event of May 2011 in Iceland, it has been positioned in the Kirkjubæjarklaustur, southern Iceland, at approximately 75 km from the Grímsvötn volcano [23]. During its operational activities in May 2011, DPX scans were set to 14 elevations angles from 0.7° to 40°. All polarimetric observables have range, azimuth, and time sampling of 0.20 km, 1°, and 10 min, respectively, and have been properly postprocessed to remove ground clutter and other impairments. A flow diagram of the VARR algorithm chain is shown in Fig. 4. The data processing steps, applied to this case study and here summarized, are well described in [23].

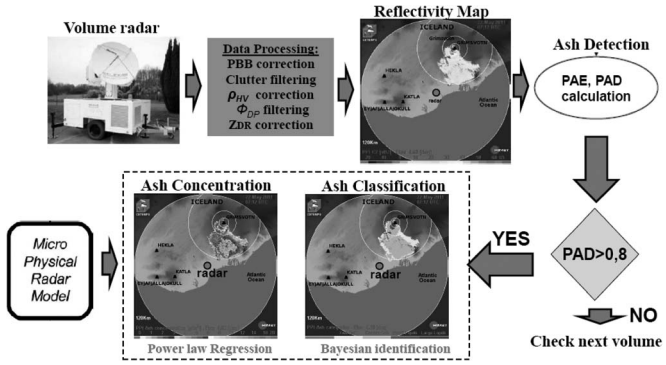

Fig. 4. VARR data processing flow diagram as applied to the 2011 Grímsvötn eruption case study (see text for details). Acronyms and symbols: PAE (probability of ash eruption), PAD (probability of ash detection), and PBB (partial beam blocking). Z_{hh} is the measured copolar reflectivity factor, Z_{dr} is the differential reflectivity, Φ_{dp} is the phase shift, and ρ_{hv} is copolar correlation (modulus).

Three concentric circular sectors, centered at the Grímsvötn eruption vent, have been set up, having maximum ranges of 8, 20, and 60 km, respectively (see Fig. 3, right panel). The number of time steps N_V, to be used in (7), depends on the rate of radar scans; since in this case scans are every 10 min, then $N_V = 6$ within an hour. The results of VAD for this case study are shown in Figs. 5 and 6 on two time intervals on the third day as an example. PAE values have been computed using the processing chain of Section II since the beginning of eruption in different weather conditions. The label value (Y'' or "N") of each sector is also shown for completeness. The maximum values of the detected reflectivity, along the vertical column centered on (i, j), are projected on the surface as a PPI georeferenced radial map. The label VMI-CZ in these figures stands for VMI-corrected reflectivity, where the corrections are those usually related to ground clutter removal and Doppler dealiasing [42].

The ash plume is visible over the Grímsvötn volcano, especially looking at the sequence of Fig. 5 where strong reflectivity

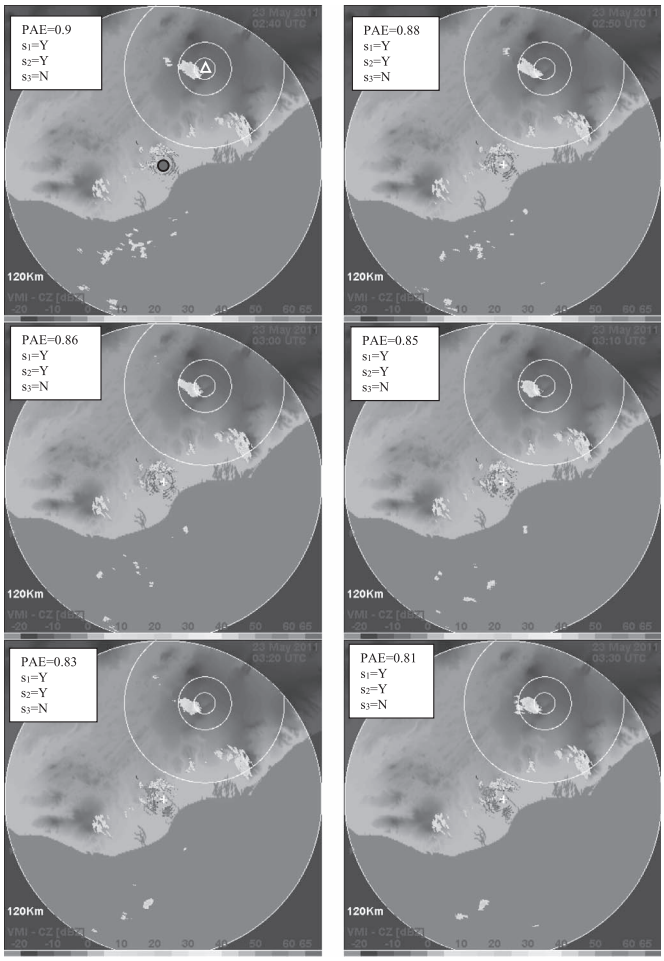

Fig. 5. VMI of corrected reflectivity (CZ), taken by Meteor 50DX on May 23 from 02:40 to 03:30 UTC during the 2011 Grímsvötn eruption. The radar and the volcano vent positions are indicated only in the first panel with the red circle and red triangle symbols, respectively. PAE and sector label values for each sector are also shown. Signals outside the s_1, s_2, and s_3 domains are mainly due to clutter.

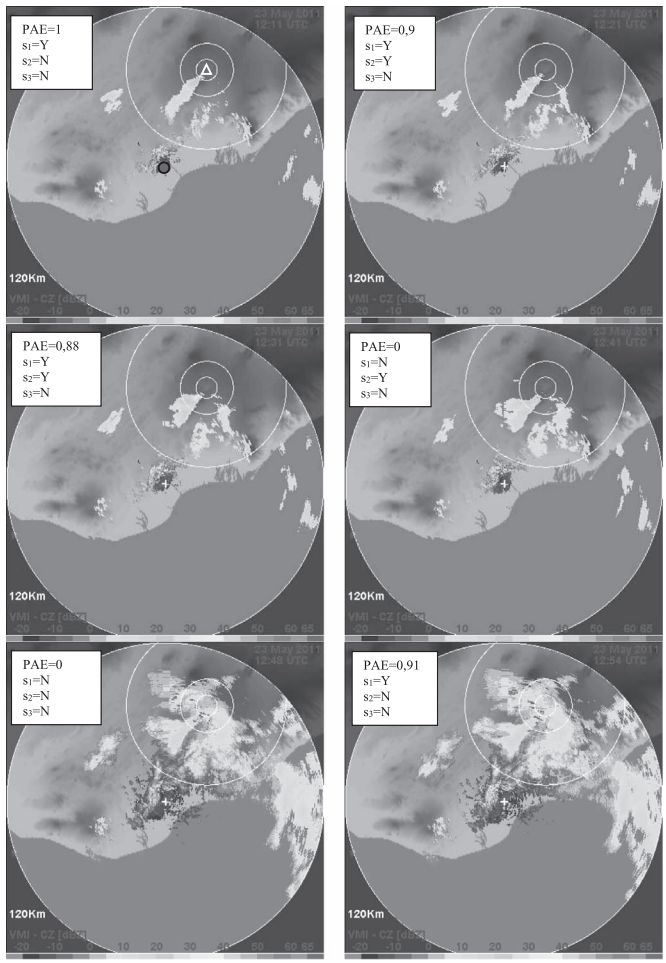

Fig. 6. Corrected VMI reflectivity images taken by Meteor 50DX on May 23 from 12:11 to 12:54 UTC during the 2011 Grímsvötn eruption. The radar and the volcano vent positions are indicated only in the first panel with the red circle and red triangle symbols, respectively. PAE and sector label values for each sector are also shown.

values are detected around the vent in clear-air conditions. On the contrary, Fig. 6 shows the sequence of PAE values in the presence of a small horizontally extended ash plume coexisting with other meteorological clouds in the outer sectors. The latter may cause false alarms, but the conditional check of all sectors avoids apparent detection errors. The detected volcanic plume is also distinguishable from undesired residual ground clutter returns, with the latter being recognizable as it tends to show a VMI stationary field from an image to another.

The temporal sequence of PAE, which might represent an operational warning product of VAD, is shown in Fig. 7 for whole days of May 24 and 25. In this figure, gray areas indicate the instants where we have found an ash plume by visual inspection of each radar scan. The colored circles in the PAD sequence refer to hit, false, and miss plume detection. The hit rate (green circles) is high, and this is an encouraging result for further tests. In the case of the 2011 Grímsvötn event, the observed temporal sequence definitely indicates a distinct ash feature erupted from the volcano vent, which can be effectively detected by means of the PAE product. Missed detection (i.e., observed but not detected by the PAE algorithm) is due to very

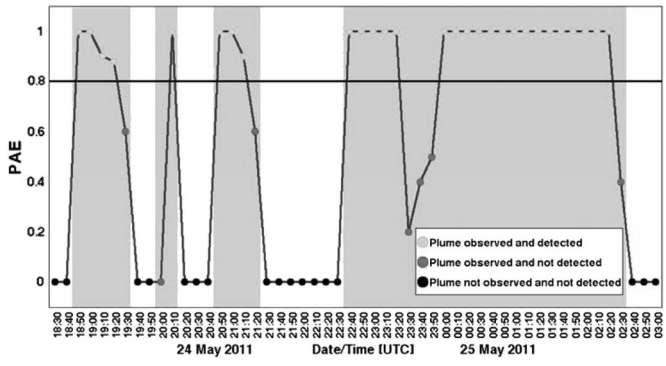

Fig. 7. Temporal sequence (sampled every 10 min) of PAE, extracted by VAD from X-band radar images on May 24–25, 2011, during the Grímsvötn eruption. Gray areas mark instants where *a posteriori* visual inspection confirmed the presence of the plume at the Grímsvötn volcano.

low reflectivity values around the volcano vent correlated to the small observed plume. False detection could instead occur when rain clouds, developing close to the volcano vent, are confused with ash plumes.

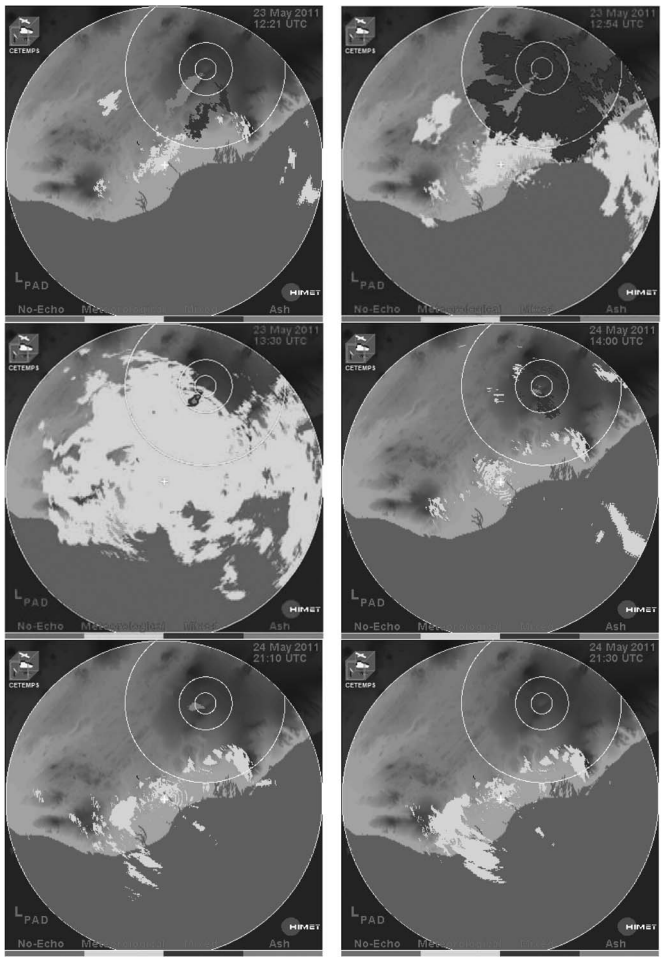

Fig. 8. Example of VAD results using the PAD label L_{PAD} for some eruption instants, selected considering different weather conditions during the 2011 Grímsvötn eruption.

Some examples of PAD results, computed by (9), are shown in Fig. 8 for some instants selected considering different weather conditions. The results are expressed using the radar detection label L_{PAD}, in (10), once setting the thresholds $T_{E3} = 0.6$ and $T_{E4} = 0.8$. As expected, in case of an ash eruption in clear air with strong reflectivity values, as in May 23 12:21 UTC, the PAD is set to *ash mode*. In the mixed scenario of May 23 13:30 UTC, the PAD changes into *uncertain mode*; it is worth noting that the residual ground clutter is classified as a meteorological target, as expected.

IV. Radar and IS Detection of Ash

MW weather radars can scan the whole atmosphere in a 3-D fashion in an area of about 10^5 km^2 [12]. The entire volume is accomplished in about 3–5 min depending on the number of elevation angles, azimuth angles, and range bins but also on the antenna rotation rate (which is typically of 3–6 rounds per min). This means that a single voxel (volume pixel) of the 3-D volume can only be sampled every few minutes. In this respect, an MW weather radar can benefit from the integration of other volcanic site measurements with a more rapid sampling but still sensitive to the onset of the ash eruption. This paragraph will explore this synergetic scenario.

The Mt. Etna volcano (Sicily, Italy) has produced more than 50 lava fountains since 2011 from a new crater formed in November 2009 [18], [25]. These events are characterized by the onset of Strombolian activity accompanied by volcanic tremor (resumption phase), an intensification of the explosions with the formation of an eruption column producing ash fallout (paroxysmal phase), and, finally, the decrease of both the explosion intensity and volcanic tremor (final phase) [20], [25].

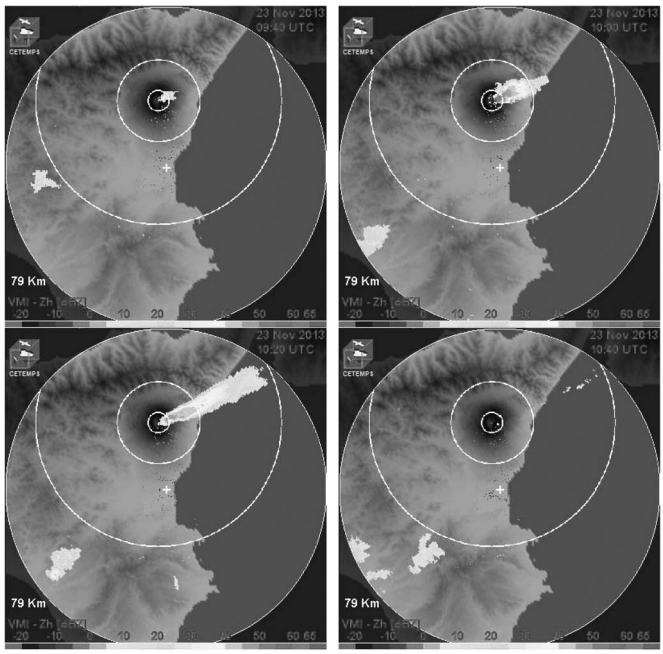

Fig. 9. VMI images, as derived from the X-band DPX radar system located at the Catania airport, during the Mt. Etna eruption on November 23, 2013. Only time steps at 9:40, 10:00, 10:20, and 10:40 UTC are shown for brevity.

The Mt. Etna eruption of November 23, 2013, was a lava fountain event more intense than usual which began in the afternoon of November 22, intensified after 07:00 UTC of November 23 [26]. The lava fountain was formed at 09:30 UTC and lasted up to 10:20 UTC, forming a magma jet up to about 1 km and an eruption plume higher than 9 km that dispersed volcanic ash toward the north-eastern volcano flanks [35]. The eruption ended at about 11:30 UTC.

This Mt. Etna eruption was observed by the same DPX X-band radar system, deployed in Iceland in 2011 (see Section III). In this case, the DPX radar is permanently positioned at the Catania airport (Sicily, Italy) at an altitude of 14 m and approximately 32 km far away from the Mt. Etna crater of interest (see Fig. 3(a), left panel). The DPX radar system works at 9.4 GHz and is operated to cover an area within a circle of 160 km radius every 10 min [23]. Fig. 9 shows the temporal samples of VMI imagery showing the onset of the lava fountain at 9:40 UTC, the intensification, and the dissipation around 10:40 UTC. Note that the ash plume is not detected by the DPX radar after 10:40 UTC since the radar is not sensitive to fine ash (with sizes less than about 50 μm diameter) at long range, which is, indeed, dispersed in the north-east direction after the eruption ended.

Volcanic activity produces infrasonic waves (i.e., acoustic waves below 20 Hz), which can propagate in the atmosphere, useful for the remote monitoring of volcanic activity [20]. IS associated with explosive eruptions is generally produced by the rapid expansion of the gas–particle mixture within the conduit, and in consequence, it is related to the dynamics of

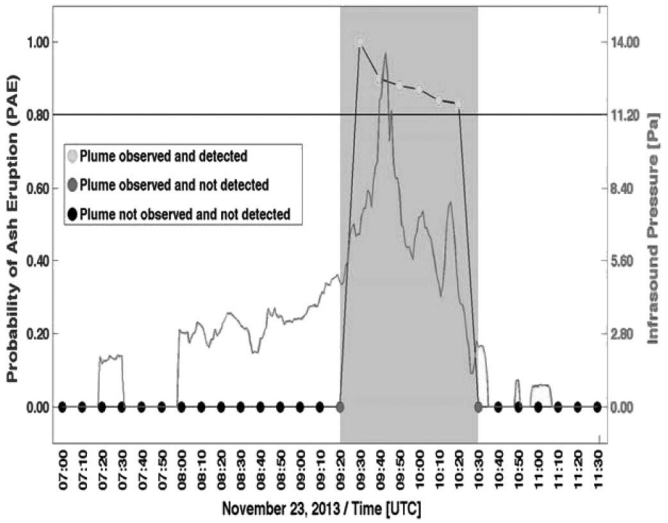

Fig. 10. Temporal sequence (blue curve) of estimated PAE, sampled every 10 min as extracted by VAD from X-band radar data, on November 23, 2013, during the Mt. Etna eruption. Gray areas mark instants where PAE was labeled "Ash," and visual inspections confirmed the presence of an ash plume. Instantaneous mean pressure from IS array (pink curve), sampled every 5 s and temporally averaged with 5-min window, is also shown.

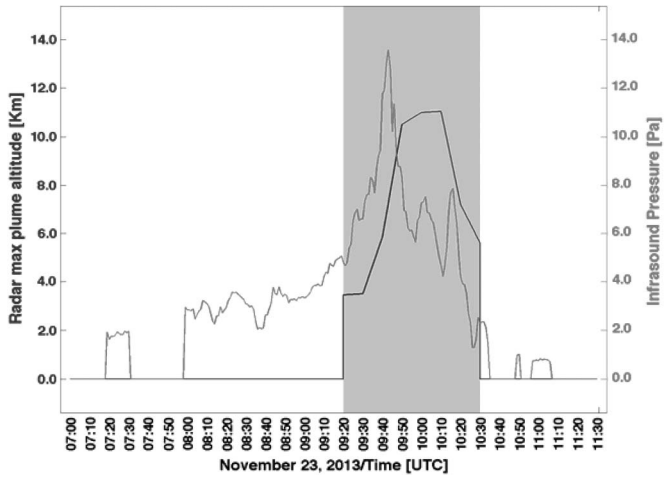

Fig. 11. Same as in Fig. 10 but for the plume maximum height above the sea level derived from VARR.

the volume outflow and thus to the intensity of the eruption [21], [22]. At Mt. Etna, a four-element IS array (with a small aperture of 120–250 m, at an elevation of 2010 m above sea level and at a distance of 5500 m from the summit craters) has been operating since 2007 [25]. Each element has a differential pressure transducer with sensitivity of 25 mV/Pa in the frequency band 0.01–50 Hz and a noise level of 10^{-2} Pa. Array analysis is performed by a multichannel semblance grid-searching procedure using a sliding 5-s long window. The expected azimuth resolution is of $\sim 2^{\circ}$, which corresponds to about 190 m at a distance of 5.5 km. The IS array mean pressure amplitude P_{ISmean} of the acoustic signals detected by the array in 5-min long time window is usually computed for data analysis. The details on this installation, operating as part of the permanent monitoring system of Etna volcano, can be found in [25].

Similar to Fig. 7, Figs. 10 and 11 show the time series of estimated PAE and plume maximum height above the sea level, respectively, derived from the VAD algorithm during the Mt. Etna eruption of November 23, 2013. Instantaneous mean pressure from infrasonic array, sampled every 5 s, is also superimposed for the same event. The interesting feature, noted in Fig. 10, is the time shift between the MW radar detection and IS signature. In particular, in this case, the time difference between the radar-based maximum height H_M and the IS-based P_{ISmean} peak is about 17 min, the VAE-based maximum plume height above the vent is about 7.9 km, and the horizontal distance up to the H_M peak from the vent is about 12 km.

This time shift between the MW radar and P_{ISmean} IS is due to the time necessary for the plume to reach its maximum height, and therefore, it is related to the plume rising velocity. Nonetheless, while IS is peaking the increase of pressure at the vent, the radar is detecting the MW maximum values above the vent. Using data shown in Figs. 10 and 11, we can thus estimate the average uprising velocity of the erupted mixture: the vertical component is about 7.7 m/s, whereas the horizontal component is about 11.7 m/s. These estimates seem to be consistent with a buoyancy-driven ascent for volcanic plumes such as that on November 23. In summary, this investigation seems to confirm the following: 1) the combination of radar and IS data is an ideal ingredient for an automatic ash eruption onset early warning within a supersite integrated system (see Fig. 1), and 2) the shift between MW radar and IS array signatures may provide an estimate of the mean buoyant plume velocity field.

V. MFR Estimation at the Volcano Vent

Once the eruption onset is detected by VAD and tracked by VAT, in order to forecast the ash dispersal, it is fundamental to estimate the source MFR at the volcano vent [28]. The plume maximum height, the vertical distribution of erupted mass, and the rate of ash injection into the atmosphere all depend on the MFR, wind entrainment and advection, temperature of the erupted mixture, and atmospheric stratification [4]. In this respect, both MW radar and IS measurements can help, and in this section, we will compare them with estimates from a parametric analytical model using data of the 2010 Eyjafjallajökull, eruption [30].

During the eruption in April to May 2010 of Eyjafjallajökull stratovolcano, the ash plume was monitored by a C-band scanning weather radar, managed by the Icelandic Meteorological Office (IMO) and located in Keflavik at 155 km from the volcano [14], [15]. The single-polarization Keflavik radar provides the reflectivity factor Z_{hhm} every 5 min. By applying the VAC and VAE of the VARR algorithm (see Fig. 1), we have obtained the ash concentration estimates for each radar bin considered above the volcano vent. The trend of the plume top height shows values between 5 and 6 km above sea level in agreement with other observations [14], [15].

A. Radar-Based and Infrasonic Retrieval of Source MFR

These VAE-based ash concentration estimates have been used to provide an approximate quantification of source MFR at the vent [31]. The evolution of a turbulent plume formed above the vent during an explosive eruption can be described physically by a mass conservation equation within a volume above the vent. By integrating over the columnar volume Vc within the closed surface S_c above the vent and using the divergence theorem, we can obtain the radar-based source MFR F_{Rrad} (in

kilograms per second) defined as the sum of derivative mass rate D_R (in kilograms per second) and the mass advection rate A_R (in kilograms per second) [31]

$$F_{\mathrm{Rrad}}(t) = D_R(t) + A_R(t) \tag{11a}$$

where, if $\mathbf{r} = [x, y, z]$ is the position vector, $\mathbf{n}_0$ is the outward normal unit vector, and $\mathbf{v}_a$ is the ash mass velocity field, it holds

$$\begin{cases} D_R(t) = \iiint_{V_c} \frac{\partial C_a(\mathbf{r},t)}{\partial t} dV \\ A_R(t) = \oint_{S_c} C_a(\mathbf{r},t)\,[\mathbf{n}_0 \cdot \mathbf{v}_a(\mathbf{r},t)]\,dS \end{cases} \tag{11b}$$

where S_c is the surface enclosing the volume V_c where the mass balance is computed.

By discretizing (11), the source MFR can be estimated from weather radar measurements around the volcano vent, imposing the time step Δt equal to the radar scan sampling time (here 5 min) and setting up the horizontal section of the columnar volume V_C (here 5×5 pixels with a pixel resampled size of about 1 km per side). The 3-D vectorial velocity field $\mathbf{v}_a(\mathbf{r}, t)$ of the divergent advection rate A_R can be estimated either from radar Doppler moments (if available) or from temporal cross-correlation techniques, such as PCORR (see Section II), applied in a 3-D fashion. If the advection rate is neglected, then MFR is underestimated as advective outflow tends to remove ash from the column.

MFR can be estimated by means of infrasonic array measurements [19]–[21]. In the far-field conditions (i.e., for acoustic wavelength much larger than source dimension), the linear theory of sound demonstrates that acoustic pressure can be related to the source outflow velocity assuming a monopole, dipole, or quadrupole source of sound [34]. Thermal camera imagery suggested that the sound associated with the Eyjafjallajökull ash plume dynamics is more consistent with the dipole source [19]. Under the assumption that the acoustic velocity of the expanding surface within the conduit is equivalent to the plume exit velocity (as suggested by thermal imagery analysis of Strombolian explosions [43]), for a cylindrical conduit of radius R_v, the IS-based source MFR F_{Rifs} can be calculated as [19]

$$F_{\mathrm{Rifs}}(t) = 6.768 \cdot \rho_p \cdot R_v^{1.66} \cdot \left(P_{\mathrm{ISmean}}(t) \frac{r_s}{\rho_{\mathrm{air}}} c \right)^{\frac{1}{3}} \tag{12}$$

where R_v is the estimated radius of the vent, ρ_p is the mixture density, P_{ISmean} is the mean pressure amplitude, ρ_{air} is the density of the atmosphere, c is the sound speed, and r_s is the distance from the source (see [19] for parameter values). For this case study, the ash plume activity of Eyjafjallajökull in 2010 has been recorded using a four-element infrasonic array at a distance of 8.3 km from the craters. These sensors were chosen for their wide frequency band, good pressure sensitivity, and low power requirement (about 60 mW). All of the array elements were connected to the central station by cables, and data were digitized and transmitted via Internet link to the IMO.

B. Analytical and Model-Based Evaluation of the Source MFR

Another way to estimate MFR from the eruptive plume top height is to resort to simplified parametric empirical formulas (e.g., [4], [6], and [36]) and analytical equations (e.g., [28]). In particular, H_M can be derived from radar scans (even though the finer particles in the upper plume can be missed due to reduced sensitivity) [14], [15], [38]. The source MFR of a volcanic plume is fundamentally related to the plume top height as a result of the dynamics of buoyant plume rise in the atmosphere but is also affected by atmosphere stratification (buoyancy frequency), cross-wind, and humidity [28], [33]. A nonlinear parametric equation to estimate F_{Rmod} has been derived to include both local cross-wind and buoyancy frequency conditions at a given instant [28]

$$F_{\mathrm{Rmod}}(t) = a_0 \left[a_1 H_M^4(t) + a_2 H_M^3(t) \right] \tag{13}$$

where a_0, a_1, and a_2 are coefficients dependent on the gravitational acceleration, air and plume density, air and plume temperature, specific heat capacity of both air and particles, buoyancy frequency, radial entrainment, wind entrainment, and wind velocity profile. The application of (13) (from now on defined as D&B analytical model) at given time step t requires that the atmospheric conditions close to the volcanic vent are known in order to evaluate the plume bending under the wind effects. Under the approximation of horizontal uniformity of free troposphere, these conditions can be derived from the closest radiosounding (RaOb) station. For this case study, atmospheric conditions obtained by ECMWF ERA-40 reanalysis at 0.25° resolution interpolated above the Eyjafjallajökull volcano (see [28, Fig. S5]). The other parameters used in (13) are listed in [28, Tables S1 and S2].

The source MFR, here labeled as $F_{\mathrm{Rnum}}(t)$, can also be derived from 1-D numerical models [28]. The latter are based on the theory of turbulent gravitational convection from a maintained volcanic source taking into account wind and humidity in the atmosphere, based on Morton's theory [37]. Results from 1-D numerical models are can be obtained by Monte Carlo simulations run over a large parameter space of source conditions (temperature, exit velocity, exsolved gas mass fraction, vent radius, and vent height), atmospheric conditions (temperature, wind, and humidity profiles), and radial and wind entrainment coefficients [28]. From this ensemble of 1-D Monte Carlo simulation, minimum and maximum values of $F_{\mathrm{Rnum}}(t)$ can be derived at each time step. For these simulations, we used the same parameters and atmospheric conditions as in (13), but we also take into account the humidity atmosphere (see [28, Fig. S5]). The source conditions used can be found in [28, Table S2].

C. Intercomparison Results

The temporal trend of the VARR-based MFR $F_{\mathrm{Rrad}}(t)$ for the period of May 5–10, 2010, is shown in Fig. 12 by comparing $F_{\mathrm{Rrad}}(t)$ obtained with and without the advection term in (11) at 10-min sampling as well as every half hour, 1 h, and 3 h. The MFR variability, as detected and estimated by the weather radar, shows a pulsed behavior of the MFR at shorter time scales [31], [32]. Note that the oscillations of VARR-based MFR estimates may be affected by the time sampling of the radar and the volume scan time interval, which is accomplished in a few minutes, whereas the ash plume parameters can vary on the order of a few seconds.

Neglecting the advection term in (10) may lead to an MFR underestimation on average less than an order of magnitude or, in terms of percentage fractional difference, larger than 100% (see middle panel of Fig. 12). This VARR-derived MFR variability is about two orders of magnitudes at 10-min sampling

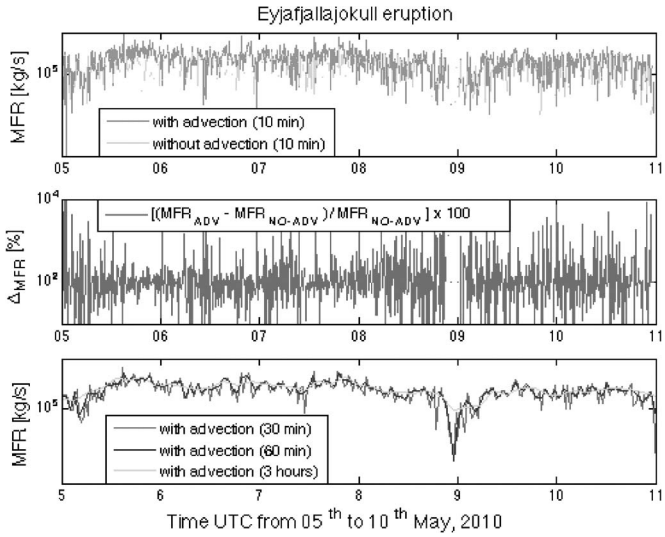

Fig. 12. (Top panel) Temporal trend of radar-derived MFR, estimated considering in (11) the A_R advection term (orange line) and without advection term (green line), within the eruption period of May 5–10, 2010. (Mid panel) Percentage fractional difference between radar-derived MFR with advection and MFR without advection term, normalized to MFR with advection. (Bottom panel) Averaged VARR-derived MFR, obtained considering the advection term, with running time windows of 30, 60, and 180 min (red, blue, and green lines, respectively).

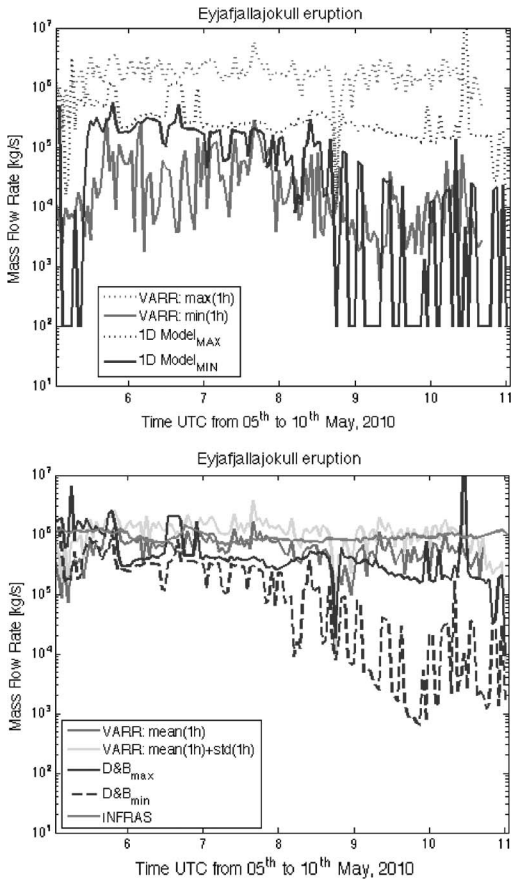

Fig. 13. (Top panel) As in Fig. 12 but showing the 1-D numerical model MFR minimum and maximum values (derived from Monte Carlo simulations using available radiosonde data) compared with the VARR-based MFR minimum and maximum values, obtained from the VARR radar algorithm within a running window of 1 h. (Bottom panel) Intercomparison among the 1-h sampled temporal trends of MFR obtained from the following: 1) VARR radar algorithm using an average of 60 min (red line) with its standard deviation (green line); 2) the D&B analytical model, applied to the minimum and maximum radar-retrieved plume heights within 1 h (blue line); and 3) IS (INFRAS) array data (pink line). See text for details.

and about an order of magnitude after 1-h averaging with a mean value around 5 10^5 kg/s within the observed period. The radar-based capability to catch the MFR intermittent behavior is, to a certain extent, expected as it closely correlates with the pulsating explosive activity through the estimate of the ash mass change and advection [32]. It is worth noting that MFR estimates from field data during the period between May 4 and 8 have provided average values between 0.6 and 2.5 10^5 kg/s [28], [30], not too far from VARR-based MFR variability around its mean value (see Fig. 12). VARR-based MFR values are also higher than those estimated by near-field video analyses between 2.2 and 3.5 10^4 kg/s [36] but closer to those derived from other plume height models between 26.2 and 43.6 10^4 kg/s [36], [33].

Fig. 13 shows the MFR temporal trends in terms of the minimum and maximum values of $F_{\mathrm{Rnum}}(t)$, derived from the Monte Carlo 1-D numerical model using radiosonde available every hour, compared to the minimum and maximum values of $F_{\mathrm{Rrad}}(t)$, derived from the VARR-based algorithm taken every 10 min within a running window of 60 min. The average value of the 1-D model MFR is about 10^5 kg/s within the observed period, whereas the minimum values are cut at 10^2 kg/s, lower values indicating that there were significant humidity effects. This only affects the minimum MFR estimate. The peak-to-peak variability of the VARR-derived estimates of MFR is typically between 10^4 and 10^6 kg/s with episodes down to 10^3 kg/s around May 9. Radar-based MFR tends to be larger than that exhibited by the 1-D numerical model, except in a few cases where the 1-D model shows much lower minimum values. These low values can be, for the most part, attributed to the strong humidity effects in the period after May 8, 2010. Due to the change in heat capacity and latent heat release associated with condensation, even plumes with very low MFRs can obtain the observed heights [28]. Additionally, there is a larger variability of the plume tops in this period, whose minimum values tend to be much lower than those before May 8.

Fig. 13 also shows the intercomparison among the 1-h sampled temporal trends of $F_{\mathrm{Rrad}}(t)$, $F_{\mathrm{Rmod}}(t)$, and $F_{\mathrm{Rifs}}(t)$, respectively, i.e., MFR estimates obtained from the VARR radar algorithm (expressed as a 1-h average together with its standard deviation), from the D&B analytical model (i.e., using (13) applied to the minimum and maximum radar-retrieved plume heights every hour; see [28] for details), from the 1-D numerical model and from infrasonic array data. Both MFR estimates of the VARR radar and IS estimates of the averaged MFR are in quite good agreement, with the IS estimate within the standard deviation of the radar-based MFR being around 10^6 kg/s. The D&B analytical model tends to provide a lower MFR especially after May 8, 2010. This behavior is strictly linked to the radar estimate of the plume top height H_M in (13), which tends to be lower in the observation period [14], [15], [29]. Indeed, radar estimates of H_M may be an underestimation of the true plume top height due to the reduced sensitivity to particle size finer than 50 μm and to the possible occlusions of observation sectors due to ground clutter.

It is also worth noting that, even at the same time sampling of 1 h, VARR-based estimates of the source MFR exhibit a higher intermittency with respect to 1-D model and IS estimates with an MFR variability larger than one order of magnitude (this variability is increased up to two orders of magnitudes at 10-min sampling in Fig. 12). This feature, which should be confirmed by future investigations, might be related to the fact that the VARR-derived MFR is strictly linked to the mass change rate and its advection, whereas 1-D model estimates depend on the plume top height (which may respond in a slower source flux changes), and IS estimates are indirectly correlated to the source MFR through the measured acoustic wave pressure. Furthermore, the uncertainty in the observed parameters of these methods is amplified by the uncertainty of the model parameters used in (12), (13), and the 1-D model. In the case of the 1-D plume model and the analytical expression (13), for example, the results can be very sensitive to the choice of entrainment coefficients [45].

VI. Conclusion

A hybrid algorithm, named VAD that exploits weather radar data, has been presented to detect the onset of the explosive volcanic eruption and estimate the MFR at the volcano vent. The VAD approach, part of the VARR methodology, can provide the PAD within the radar coverage area and the PAE at the fissure. Estimates of PAE have been provided for two eruption case studies, namely, in Iceland on 2011 and in Italy in 2013. The quantitative analysis shows very encouraging results in terms of detection and labeling which can be useful for any support decision system dealing with volcanic eruption hazard. The PAE index can be usefully exploited as a diagnostic tool for an early-warning integrated platform, which can be of interest for civil prevention and protection. Assuming to pursue a self-consistent radar approach, a way to improve PAE is to also exploit in case of uncertain labeling: 1) spatial texture of ash field radar observables versus rain field around the volcano vent; 2) temporal evolution of the radar observables around the volcano vent; 3) Doppler spectrum (mean and spectral width) variability in time and space around the volcano vent; 4) vertical section (RHI) of measured reflectivity along the radar-vent cross section; 5) detection of a strong reflectivity gradient (both in space and time) due to ash cloud; and 6) use of some polarimetric observables, such as Z_{dr}, since, for tumbling ash particles, $Z_{dr} \approx 0$ for any concentration and diameter, whereas for strong reflectivity, ash may have K_{dp} values near or less than zero as opposed to rainfall. The correlation coefficient should have low values above and around the volcano vent in case of eruption being a great mixture of nonspherical particles.

This work has also explored, using the Italian case study in 2013, the synergy between MW weather radars and infrasonic array observations. The latter have been already used for detecting Etna lava fountains with a high degree of confidence, thus demonstrating to be an essential tool for volcanic eruption early warning. Before designing an integrated tool, the interpretation of the respective signatures needs to be investigated, and this has been the goal of the presented analysis. Results indicate that the response of the weather radar and infrasonic array to the eruption onset of the plume is correlated and characterized by a time lapse due to the plume rise. The different time samplings of the two measurements, typically 10 and 1 min for radar and IS, respectively, should be taken into consideration when trying to derive eruption dynamical parameters. If confirmed by further case analyses, the synergy of weather radar and infrasonic array can be framed within the VAD hybrid algorithm by introducing a proper conditional probability of PAE driven by infrasonic array data. This may help VAD to remove ambiguous mixed-phase conditions where the ash plume is coexisting with the meteorological clouds.

Finally, VARR-based retrievals of the source MFR at the vent have been analyzed for a further event in Iceland in 2010 by comparing them with the estimates of a 1-D numerical model, an analytical formula, and infrasonic array data. The estimate of the source MFR is considered a fundamental step in characterizing the volcanic source but very difficult to measure accurately. Thus, this work for the first time has proposed the intercomparison between two experimental techniques, based on weather radar and infrasonic array data, supported by the analyses of two modeling approaches. The results show a substantial agreement about the average estimate of MFR from both instruments, with the VARR-based showing a larger variability probably due to the source pulse intermittency. The 1-D model variability is within the peak-to-peak estimate of VARR, whereas the wind-driven analytical model can underestimate MFR due to the limits in the estimation of top plume height by the radar. A 5-min time resolution appears to be a good compromise to estimate the 1-h average MFR and its standard deviation and to allow a complete volume radar scan.

Further work is required to assess the usefulness of VAD on a statistical basis using a significant number of case studies as well as to couple it with collocated infrasonic array pressure measurements. Unfortunately, only few volcanic sites are nowadays equipped with both instruments, and the historical data set is very limited so far. The PAE value and relative spatial identification by means of synergetic PAE and PAD values can be displayed continuously on a devoted web site. Positions of potentially active volcanoes should be displayed as an overlay on monitoring screens. Seismic data can complement the VARR scheme as *a priori* data in the VAD radar detection module. We expect them to be less correlated to the eruption onset, but they can corroborate and increase the VAD probability of detection. L-band Doppler radar monitoring with a fixed beam aiming near the source can be easily ingested in the detection procedure (an example can be the Voldorad L-band system near the Etna volcano). Other data, coming from ground-based and space-based remote sensors, can be also combined within VARR in order to provide a comprehensive quantitative overview of the evolving eruption scenario and its source parameters, useful for supporting the decisions of the interested Volcanic Ash Advisory Center.

Acknowledgment

The authors would like to thank B. Pálmason, H. Pétursson, and S. Karlsdóttir (IMO, Iceland) for providing the X- and C-band Iceland radar data and G. Vulpiani and P. Pagliara (DPC, Italy) for providing the X-band Italian radar data. The application of VARR chain algorithms, developed in C language and MATLAB environment, can be discussed with the authors upon request.

REFERENCES

[1] T. P. Miller and T. J. Casadevall, "Volcanic ash hazards to aviation," in *Encyclopedia of Volcanoes*, H. Sigurdsson, B. F. Houghton, S. R. McNutt, H. Rymer, and J. Stix, Eds. San Diego, CA, USA: Academic, 2000, pp. 915–930.

[2] M. O'Regan, "On the edge of chaos: European aviation and disrupted mobilities," *Mobilities*, vol. 6, no. 1, pp. 21–30, 2011.

[3] A. J. Prata and A. Tupper, "Aviation hazards from volcanoes: The state of the science," *Natural Hazards*, vol. 51, no. 2, pp. 239–244, Nov. 2009, doi: 10.1007/s11069-009-9415-y.

[4] R. S. J. Sparks *et al.*, *Volcanic Plumes*. New York, NY, USA: Wiley, 1997.

[5] A. Stohl *et al.*, "Determination of time- and height-resolved volcanic ash emissions and their use for quantitative ash dispersion modeling: The 2010 Eyjafjallajökull eruption," *Atmos. Chem. Phys.*, vol. 11, pp. 4333–4351, May 2011.

[6] L. G. Mastin *et al.*, "A multidisciplinary effort to assign realistic source parameters to models of volcanic ash-cloud transport and dispersion during eruptions," *J. Volcanol. Geothermal Res.*, vol. 186, no. 1, pp. 10–21, Sep. 2009.

[7] W. I. Rose, G. J. S. Bluth, and G. G. J. Ernst, "Integrating retrievals of volcanic cloud characteristics from satellite remote sensors: A summary," *Philos. Trans. Roy. Soc.*, vol. A358, no. 1770, pp. 1538–1606, May 2000.

[8] A. J. Prata and I. F. Grant, "Retrieval of microphysical and morphological properties of volcanic ash plumes from satellite data: Application to Mt. Ruapehu, New Zealand," *Q. J. Roy. Meteorol. Soc.*, vol. 127, no. 576, pp. 2153–2179, Jul. 2001.

[9] M. J. Pavolonis, W. F. Feltz, A. K. Heidinger, and G. M. Gallina, "A daytime complement to the reverse absorption technique for improved automated detection of volcanic ash," *J. Atmos. Ocean. Technol.*, vol. 23, no. 11, pp. 1422–1444, Nov. 2006.

[10] D. M. Harris and W. I. Rose, "Estimating particle sizes, concentrations, and total mass of ash in volcanic clouds using weather radar," *J. Geophys. Res.*, vol. 88, no. C15, pp. 10 969–10 983, Dec. 1983.

[11] C. Lacasse, S. Karlsdóttir, G. Larsen, H. Soosalu, W. I. Rose, and G. G. J. Ernst, "Weather radar observations of the Hekla 2000 eruption cloud," *Bull. Volcanol.*, vol. 66, no. 5, pp. 457–473, Jul. 2004.

[12] F. S. Marzano, E. Picciotti, G. Vulpiani, and M. Montopoli, "Inside volcanic clouds: Remote sensing of ash plumes using microwave weather radars," *Bull. Amer. Meteorol. Soc.*, vol. 94, pp. 1567–1586, Oct. 2013.

[13] F. S. Marzano, S. Barbieri, E. Picciotti, and S. Karlsdóttir, "Monitoring sub-glacial volcanic eruption using C-band radar imagery," *IEEE Trans. Geosci. Remote Sens.*, vol. 48, no. 1, pp. 403–414, Jan. 2010.

[14] F. S. Marzano, M. Lamantea, M. Montopoli, S. Di Fabio, and E. Picciotti, "The Eyjafjallajökull explosive volcanic eruption from a microwave weather radar perspective," *Atmos. Chem. Phys.*, vol. 11, pp. 9503–9518, 2011.

[15] P. Arason, G. N. Petersen, and H. Bjornsson, "Observations of the altitude of the volcanic plume during the eruption of Eyjafjallajökull, April–May 2010," *Earth Syst. Sci. Data*, vol. 3, no. 1, pp. 9–17, Sep. 2011.

[16] F. S. Marzano, S. Barbieri, G. Vulpiani, and W. I. Rose, "Volcanic ash cloud retrieval by ground-based microwave weather radar," *IEEE Trans. Geosci. Remote Sens.*, vol. 44, no. 11, pp. 3235–3246, Nov. 2006.

[17] F. S. Marzano, E. Picciotti, G. Vulpiani, and M. Montopoli, "Synthetic signatures of volcanic ash cloud particles from X-band dual-polarization radar," *IEEE Trans. Geosci. Remote Sens.*, vol. 50, no. 1, pp. 193–211, Jan. 2012.

[18] S. Scollo, M. Prestifilippo, G. Spata, M. D. Agostino, and M. Coltelli, "Monitoring and forecasting Etna volcanic plumes," *Nature Hazards Earth Syst. Sci.*, vol. 9, pp. 1573–1585, 2009.

[19] M. Ripepe, C. Bonadonna, A. Folch, D. Delle Donne, G. Lacanna, and B. Voight, "Ash-plume dynamics and eruption source parameters by infrasound and thermal imagery: The 2010 Eyjafjallajokull eruption," *Earth Planet. Sci. Lett.*, vol. 366, pp. 112–121, Mar. 2013, doi: 10.1016/j.epsl.2013.02.005.

[20] J. B. Johnson, R. C. Aster, and P. R. Kyle, "Volcanic eruptions observed with infrasound," *Geophys. Res. Lett.*, vol. 31, no. 14, Jul. 2004, Art. no. L14604.

[21] J. Caplan-Auerbach, A. Bellesiles, and J. K. Fernandes, "Estimates of eruption velocity and plume height from infrasonic recordings of the 2006 eruption of Augustine Volcano Alaska," *J. Volcanol. Geothermal Res.*, vol. 189, no. 1/2, pp. 12–18, Jan. 2010, doi: 10.1016/j.jvolgeores.2009.10.002.

[22] M. Ripepe, S. De Angelis, G. Lacanna, and B. Voight, "Observation of infrasonic and gravity waves at Soufrière Hills Volcano, Monserrat," *Geophys. Res. Lett.*, vol. 37, no. 19, Oct. 2010, Art. no. L00E14, doi: 10.1029/2010GL042557.

[23] M. Montopoli, G. Vulpiani, D. Cimini, E. Picciotti, and F. S. Marzano, "Interpretation of observed microwave signatures from ground dual polarization radar and space multi frequency radiometer for the 2011 Grímsvötn volcanic eruption," *Atmos. Meas. Tech.*, vol. 7, pp. 537–552, 2014.

[24] F. S. Marzano, M. Lamantea, M. Montopoli, B. Oddsson, and M. T. Gudmundsson, "Validating sub-glacial volcanic eruption using ground-based C-band radar imagery," *IEEE Trans. Geosci. Remote Sens.*, vol. 50, no. 4, pp. 1266–1282, Apr. 2012.

[25] G. Ulivieri, M. Ripepe, and E. Marchetti, "Infrasound reveals transition to oscillatory discharge regime during lava fountaining: Implication for early warning," *Geophys. Res. Lett.*, vol. 40, no. 12, pp. 3008–3013, Jun. 2013.

[26] S. Corradini *et al.*, "A multi-sensor approach for the volcanic ash cloud retrievals and eruption characterization," *Remote Sens.*, vol. 8, no. 1, p. 58, Jan. 2016.

[27] F. S. Marzano, M. Lamantea, M. Montopoli, M. Herzog, H. Graf, and D. Cimini, "Microwave remote sensing of the 2011 Plinian eruption of the Grímsvötn Icelandic volcano," *Remote Sens. Environ.*, vol. 129, pp. 168–184, Feb. 2013.

[28] W. Degruyter and C. Bonadonna, "Improving on mass flow rate estimates of volcanic eruptions," *Geophys. Res. Lett.*, vol. 39, no. 16, Aug. 2012, Art. no. L16308.

[29] H. Bjornsson, S. Magnusson, P. Arason, and G. N. Petersen, "Velocities in the plume of the 2010 Eyjafjallajökull eruption," *J. Geophys. Res. Atmos.*, vol. 118, no. 20, pp. 11 698–11 711, Oct. 2013, doi: 10.1002/jgrd.50876.

[30] C. Bonadonna *et al.*, "Tephra sedimentation during the 2010 Eyjafjallajokull eruption (Iceland) from deposit, radar, and satellite observations," *J. Geophys. Res.*, vol. 116, no. B12, Dec. 2011, Art. no. B12202.

[31] L. Mereu, F. S. Marzano, M. Montopoli, and C. Bonadonna, "Retrieval of tephra size spectra and mass flow rate from C-band radar during the 2010 Eyjafjallajökull eruption, Iceland," *IEEE Trans. Geosci. Remote Sens.*, vol. 53, no. 10, pp. 5644–5660, Oct. 2015.

[32] E. Kaminski, S. Tait, F. Ferrucci, M. Martet, B. Hirn, and P. Husson, "Estimation of ash injection in the atmosphere by basaltic volcanic plumes: The case of the Eyjafjallajokull 2010 eruption," *J. Geophys. Res.*, vol. 116, no. B9, Sep. 2011, Art. no. B00C02.

[33] M. J. Woodhouse, A. J. Hogg, J. C. Phillips, and R. S. J. Sparks, "Interaction between volcanic plumes and wind during the 2010 Eyjafjallajökull eruption, Iceland," *J. Geophys. Res. Solid Earth*, vol. 118, pp. 92–109, 2013.

[34] M. J. Lighthill, *Waves in Fluids*. New York, NY, USA: Cambridge Univ. Press, 1978, p. 504.

[35] D. Andronico, S. Scollo, and A. Cristaldi, "Unexpected hazards from tephra fallouts at Mt Etna: The 23 November 2013 lava fountain," *J. Volcanol. Geothermal Res.*, vol. 304, pp. 118–125, 2015.

[36] T. Dürig *et al.*, "Mass eruption rates in pulsating eruptions estimated from video analysis of the gas thrust-buoyancy transition—A case study of the 2010 eruption of Eyjafjallajökull, Iceland," *Earth, Planets Space*, vol. 67, p. 180, 2015.

[37] B. R. Morton, G. T. Taylor, and J. S. Turner, "Turbulent gravitational convection from maintained and instantaneous sources," *Proc. Roy. Soc. London, A, Math. Phys. Eng. Sci.*, vol. 234, no. 1196, pp. 1–23, Jan. 1956.

[38] B. Oddsson, M. T. Gudmundsson, G. Larsen, and S. Karlsdóttir, "Monitoring of the plume from the basaltic phreatomagmatic 2004 Grímsvötn eruption—Application of weather radar and comparison with plume models," *Bull. Volcanol.*, vol. 74, no. 6, pp. 1395–1407, 2012.

[39] A. R. Van Eaton *et al.*, "Hail formation triggers rapid ash aggregation in volcanic plumes," *Nature Commun.*, vol. 6, 2015, Art. no. 7860.

[40] G. N. Petersen, H. Bjornsson, P. Arason, and S. Von Löwis, "Two weather radar time series of the altitude of the volcanic plume during the May 2011 eruption of Grímsvötn, Iceland," *Earth Syst. Sci. Data*, vol. 4, no. 1, pp. 121–127, 2012.

[41] M. Montopoli, F. S. Marzano, E. Picciotti, and G. Vulpiani, "Spatially-adaptive advection radar technique for precipitation mosaic nowcasting," *IEEE J. Sel. Topics Appl. Remote Sens.*, vol. 3, pp. 874–884, Jun. 2012.

[42] H. Sauvageot, *Radar Meteorology*. Norwood, MA, USA: Artech House, 1992.

[43] D. DelleDonne and M. Ripepe, "High-frame rate thermal imagery of Strombolian explosion: Implication of infrasonic source dynamics," *J. Geophys. Res.*, vol. 117, no. B9, 2012, Art. no. B09206.

[44] M. Montopoli, "Velocity profiles inside volcanic clouds from three-dimension scanning microwave dual polarization Doppler radars," *J. Geophys. Res.—Atmos.*, to be published.

[45] C. Bonadonna, M. Pistolesi, R. Cioni, W. Degruyter, M. Elissondo, and V. Baumann, "Dynamics of wind-affected volcanic plumes: The example of the 2011 Cordón Caulle eruption, Chile," *J. Geophys. Res. Solid Earth*, vol. 120, pp. 2242–2261, 2015.

Frank S. Marzano (S'89–M'99–SM'03–F'15) received the Laurea degree (*cum laude*) in electrical engineering and the Ph.D. degree in applied electromagnetics from the University of Rome "La Sapienza," Rome, Italy, in 1988 and 1993, respectively.

In 1992, he was a Visiting Scientist with Florida State University, Tallahassee, FL, USA. In 1993, he collaborated with the Institute of Atmospheric Physics, National Council of Research (CNR), Rome. From 1994 to 1996, he was a Postdoctorate Researcher with the Italian Space Agency, Rome. After being a Lecturer with the University of Perugia, Perugia, Italy, in 1997, he joined the Department of Electrical Engineering, University of L'Aquila, L'Aquila, Italy, teaching courses on electromagnetic fields as an Assistant Professor. In 1999, he was a Visiting Scientist with the Naval Research Laboratory, Monterey, CA, USA. In 2002, he got the qualification to Associate Professorship and cofounded the Center of Excellence on Remote Sensing and Hydro-Meteorological Modeling (CETEMPS), L'Aquila. In 2005, he finally joined the Department of Information Engineering, Electronics and Telecommunications, Sapienza University of Rome, Rome, where he currently teaches courses on antennas, propagation, and remote sensing. Since 2007, he has been the Vice-Director of CETEMPS, University of L'Aquila, where he became the Director in 2013. He has published more than 110 papers on refereed international journals, more than 30 contributions to international book chapters, and more than 230 extended abstract on international and national congress proceedings. He was the editor of two books. His current research concerns passive and active remote sensing of the atmosphere from ground-based, airborne, and spaceborne platforms and electromagnetic propagation studies.

Dr. Marzano has been an Associate Editor of the IEEE GEOSCIENCE REMOTE SENSING LETTERS since January 2004. In 2005 and 2007, he was a Guest Coeditor of the MicroRad04 and MicroRad06 Special Issues for IEEE-GRSL. Since January 2011, he has been an Associate Editor of the journal *EGU Atmospheric Measurements Techniques*. He is a Fellow of IEEE and the Royal Meteorological Society and a member of the MWI-ICI Science Advisory Group of the EuMetSat and PMM Science Team of NASA.

Errico Picciotti received the Laurea degree (*cum laude*) in electrical engineering from the University of Ancona, Ancona, Italy, in 1993.

In 1997, he was a Radar Meteorologist with the Science and Technology Park of Abruzzo, L'Aquila, Italy. In 2002, he was a Researcher with the CETEMPS, University of L'Aquila, L'Aquila, where he worked on radar systems and polarimetry. Since 2007, he has been with HIMET, L'Aquila, where he is the Manager of the Radar Meteorology Division. His main research interests are devoted to radar meteorology and volcanic plume retrieval algorithms.

Saverio Di Fabio received the Laurea degree in electrical engineering from the University of L'Aquila, L'Aquila, Italy.

In 1998, he joined the Science and Technology Park of Abruzzo, L'Aquila, as a Microwave Engineer. From 2009 to 2012, he was a Radar Engineer with HIMET, L'Aquila. Since 2012, he has been a Senior Scientist with CETEMPS, University of L'Aquila, where he has been working on radar systems and polarimetric data processing.

Mario Montopoli received the Laurea degree in electronic engineering from the University of L'Aquila, L'Aquila, Italy, in 2004 and the Ph.D. degree in radar meteorology under a joint program from the University of Basilicata, Potenza, Italy, and Sapienza University of Rome, Rome, Italy, in 2008.

In 2005, he joined the Center of Excellence CETEMPS as a Research Scientist on ground-based radar meteorology and microwave remote sensing. In 2006, he was a Research Assistant with the Department of Electrical Engineering and Information, University of L'Aquila. From October 2011 to 2013, he was with the Department of Geography, University of Cambridge, Cambridge, U.K., under the Marie Curie FP7 European program. He is currently with the Department of Information Engineering, Sapienza University of Rome, and a EuMetSat Visiting Scientist with the H-SAF facility.

Luigi Mereu received the B.Sc. and M.Sc. degrees in telecommunication engineering from Sapienza University of Rome, Rome, Italy, in 2007 and 2012, respectively.

In 2012, he joined the Department of Information Engineering, Sapienza University of Rome, and the Centre of Excellence CETEMPS, L'Aquila, Italy, to cooperate on radar remote sensing of volcanic ash clouds within the ICT Ph.D. program. He has been involved in the FUTUREVOLC European project that started in 2012.

Mr. Mereu received the IEEE GRS South Italy Award for the Best Master's Thesis in remote sensing in 2012.

Wim Degruyter received the M.Eng.Sci. degree from the University of Ghent, Gent, Belgium, in 2006 and the Ph.D. degree in earth science from the University of Geneva, Geneva, Switzerland, in 2010.

He is currently a Senior Scientist with the Institute of Geochemistry and Petrology, Department of Earth Sciences, Zurich, Switzerland. He has been a Postdoctoral Researcher with the University of California, Berkeley, CA, USA. He was a Postdoctoral Researcher with Georgia Institute of Technology, Atlanta, GA, USA, from 2010 to 2015. His main research interests are devoted to the development of 1-D models to simulate bubble growth, magma chamber dynamics, magma ascent dynamics, and volcanic plume behavior.

Costanza Bonadonna received the B.S. degree in geology from the University of Pisa, Pisa, Italy, and the Ph.D. degree from the University of Bristol, Bristol, U.K.

She is an Associate Professor with the Department of Earth Sciences, University of Geneva, Geneva, Switzerland, and the Head of the CERG-C Program for the Assessment and Management of Geological and Climate Related Risk. She was then awarded the position of SOEST Young Investigator at the University of Hawaii, Honolulu, HI, USA, for two years and was later appointed the position of Assistant Professor at the University of South Florida, Tampa, FL, USA. She has devoted most of her research to modeling sedimentation from volcanic plumes, exploring new methodologies for the characterization of tephra-fall deposits, and developing probabilistic analyses for the assessment of tephra-fall hazards. She is now also involved in several multidisciplinary projects for the quantification of risk.

Dr. Bonadonna was a recipient of the President's Award of the Geological Society of London in 2001, the IAVCEI Outstanding Recent Graduate (George Walker Award) in 2004, the Outstanding Woman in Science Award of the Geological Society of America in 2004, and the USF Outstanding Faculty Research Achievement Award in 2005.

Maurizio Ripepe received the Laurea degree in geological sciences from the University of Florence, Florence, Italy, in 1978.

Since 1983 he has been with the Department of Earth Science, University of Florence, Florence, Italy, teaching earth physics and volcanic hazard. He was a Lecturer of geophysics and seismology with the University of Camerino, Camerino, Italy, and University of Siena, Siena, Italy (1993–2005), an External Professor with the Open University, Milton Keynes, U.K. (2001–2004), a Visiting Fellow with the University of Southern California, Los Angeles, CA, USA (1986–1989), and a Visiting Professor with the University of Hokkaido, Sapporo, Japan (2000), Ecole Normal Superioure de Physique, Lyon, France (2002), University of Tohoku, Sendai, Japan (2007), and Earthquake Research Institute, Tokyo, Japan (2009). He was also an Affiliated Researcher with the Earthquake Research Institute (ERI), Tokyo (2011). His main research interests are within geophysics and volcanology, with a focus on volcanic plumes, volcanic hazard, infrasound techniques, and field campaign activities.